

# An Adsorbate Discriminatory Gate Effect in a Flexible Porous Coordination Polymer for Selective Adsorption of CO<sub>2</sub> over C<sub>2</sub>H<sub>2</sub>

Maw Lin Foo,<sup>†,+</sup> Ryotaro Matsuda,<sup>\*,†,‡,§,||</sup> Yuh Hijikata,<sup>⊥</sup> Rajamani Krishna,<sup>#</sup> Hiroshi Sato,<sup>†</sup> Satoshi Horike,<sup>∇</sup> Akihiro Hori,<sup>†,||</sup> Jingui Duan,<sup>†</sup> Yohei Sato,<sup>||,○</sup> Yoshiki Kubota,<sup>||,○</sup> Masaki Takata,<sup>||,¶</sup> and Susumu Kitagawa<sup>\*,†,||,∇</sup>

<sup>†</sup>Institute for Integrated Cell-Material Sciences (WPI-iCeMS), Kyoto University, Yoshida, Sakyo-ku, Kyoto 606-8501, Japan

<sup>‡</sup>Department of Applied Chemistry, Graduate School of Engineering, Nagoya University, Chikusa-ku, Nagoya 464-8603, Japan

<sup>§</sup>Japan Science and Technology Agency (JST), PRESTO, 4-1-8 Honcho, Kawaguchi, Saitama 332-0012, Japan

<sup>||</sup>RIKEN SPring-8 center, 1-1-1 Kouto, Sayo-cho, Sayo-gun, Hyogo 679-5148, Japan

<sup>⊥</sup>Institute of Transformative Bio-Molecules (WPI-ITbM), Nagoya University, Chikusa-ku, Nagoya 464-8602, Japan

<sup>#</sup>Van 't Hoff Institute for Molecular Sciences, University of Amsterdam, Science Park 904, 1098 XH Amsterdam, The Netherlands

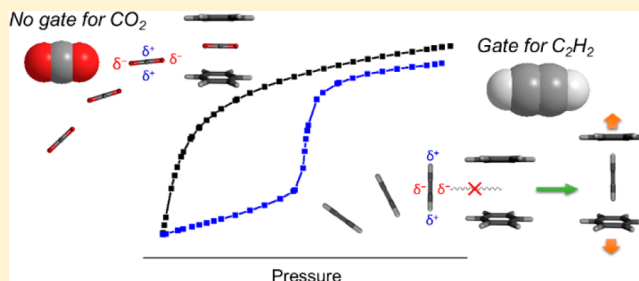
<sup>∇</sup>Department of Synthetic Chemistry and Biological Chemistry, Graduate School of Engineering, Kyoto University, Katsura, Nishikyo-ku, Kyoto 615-8510, Japan

<sup>○</sup>Department of Physical Science, Graduate School of Science, Osaka Prefecture University, 1-1 Gakuen-cho, Naka-ku, Sakai, Osaka 599-8531, Japan

<sup>¶</sup>Institute of Multidisciplinary Research for Advanced Materials, Tohoku University, 2-1-1 Katahira, Aoba-ku, Sendai 980-8577, Japan

## Supporting Information

**ABSTRACT:** The adsorptive separation of C<sub>2</sub>H<sub>2</sub> and CO<sub>2</sub> via porous materials is nontrivial due to the close similarities of their boiling points and kinetic diameters. In this work, we describe a new flexible porous coordination polymer (PCP) [Mn(bdc)(dpe)] (H<sub>2</sub>bdc = 1,4-benzenedicarboxylic acid, dpe = 1,2-di(4-pyridyl)ethylene) having zero-dimensional pores, which shows an adsorbate discriminatory gate effect. The compound shows gate opening type abrupt adsorption for C<sub>2</sub>H<sub>2</sub> but not for CO<sub>2</sub>, leading to an appreciable selective adsorption of CO<sub>2</sub> over C<sub>2</sub>H<sub>2</sub> at near ambient temperature (273 K). The origin of this unique selectivity, as unveiled by in situ adsorption-X-ray diffraction experiments and density functional theory calculations, is due to vastly different orientations between the phenylene ring of bdc and each gas in the nanopores. The structural change by photochemical transformation of this PCP via [2 + 2] photodimerization leads to the removal of inverse CO<sub>2</sub>/C<sub>2</sub>H<sub>2</sub> selectivity, verifying the mechanism of the guest discriminatory gate effect.



## INTRODUCTION

There has been considerable interest in adsorptive separations involving separation of CO<sub>2</sub> from C<sub>2</sub>H<sub>2</sub> due to its industrial relevance and scientific challenge. C<sub>2</sub>H<sub>2</sub> is an industrial gas with applications such as oxyacetylene in welding/cutting and production of chemicals such as vinyl chloride, acrylic acid, and 1,4-butanediol.<sup>1</sup> In its manufacture via partial oxidation or hydrocarbon steam cracking of hydrocarbons, CO<sub>2</sub> is an important impurity. However, it is noted that the adsorptive separation of CO<sub>2</sub> (molecular size: 3.4 × 3.4 × 5.3 Å<sup>3</sup>, bp 194.7 K) and C<sub>2</sub>H<sub>2</sub> (molecular size: 3.4 × 3.4 × 5.5 Å<sup>3</sup>, bp 189.3 K) is especially challenging due to their similarities in equilibrium sorption parameters, physicochemical properties, molecular size and shape (Table S1). In a few successful reports, porous materials were typically designed to preferentially adsorb C<sub>2</sub>H<sub>2</sub>

over CO<sub>2</sub> by utilizing adsorbent/adsorbate interactions via acid–base interaction at functional sites with highly polarizable π-electrons and acidic hydrogens on C<sub>2</sub>H<sub>2</sub>.<sup>2</sup> On the other hand, preferential adsorption of CO<sub>2</sub> over C<sub>2</sub>H<sub>2</sub> (hereafter we call it “inverse selectivity”)<sup>3</sup> is rarely observed above cryogenic temperatures, except recently in the case of a polyoxometallate hybrid ionic crystal.<sup>4</sup> However, the origins of the observed inverse selectivity were not well understood.

A unique characteristic of porous coordination polymers (PCPs) or metal–organic frameworks (MOFs)<sup>5</sup> from other conventional porous materials such as zeolites and porous carbons is structural flexibility<sup>6</sup> based on the concept of the soft

Received: October 7, 2015

Published: February 15, 2016

porosity,<sup>7</sup> providing unusual sorption behaviors. In particular, flexible PCPs in certain cases exhibit gated adsorption,<sup>8</sup> which is a unique phenomenon in which adsorption is negligible before a certain gate opening pressure ( $P_{go}$ ), but at  $P_{go}$ , an abrupt increase in adsorption occurs due to a concomitant change in pore structure induced by structural distortion. Gated adsorption is one of the unique physical properties of PCPs with possible practical applications in selective adsorption<sup>9</sup> and sensing of gas molecules.<sup>10</sup> Although some recent studies have provided some guidelines in understanding and designing structural flexibility for controlling  $P_{go}$ ,<sup>11</sup> currently there is no clear strategy established for constructing a flexible PCP which shows gated adsorption for a specific guest molecule.

With this background, we target to construct a new PCP which shows gated adsorption for a specific guest molecule (acetylene) to achieve rational inverse selectivity. In our strategy, we utilize a PCP with small zero-dimensional (0-D) pores which will interact significantly differently with CO<sub>2</sub> and C<sub>2</sub>H<sub>2</sub> due to the different signs of their quadrupole moments leading to different CH- $\pi$  and  $\pi$ - $\pi$  interactions.<sup>12</sup> Note that in larger pores, the same interactions might exist but will be markedly less in magnitude compared to isolated small 0-D pores.

Here, we show a design and synthesis of such a PCP as embodied by [Mn(bdc)(dpe)] $\Delta$ DMF ( $\Delta$ DMF) (where H<sub>2</sub>bdc = 1,4-benzenedicarboxylic acid and dpe = 1,2-di(4-pyridyl)ethylene). **1'** (**1'** = desolvated  $\Delta$ DMF) shows gate opening type abrupt adsorption for C<sub>2</sub>H<sub>2</sub> but not for CO<sub>2</sub> at low temperatures such as 195 K, leading to an appreciable selective adsorption of CO<sub>2</sub> over C<sub>2</sub>H<sub>2</sub> at near ambient temperature (273 K). In addition, to verify the mechanism of selective gate opening behavior, [2 + 2] photodimerization on **1'** was employed for fine-tuning the spatial transformation of nanospace. Indeed, the photodimerized PCP [Mn<sub>2</sub>(bdc)<sub>2</sub>(*rctt*-*tpcb*)] (**2**) (where *rctt*-*tpcb* = *regio-cis*, *trans*, *trans*-tetrakis(4-pyridyl)cyclobutane) exhibits no selectivity because of the loss of efficient interaction between CO<sub>2</sub> and pore surface, verifying the mechanism of the guest discriminatory gate effect.

## EXPERIMENTAL SECTION

All chemicals were used as received without any purification. Elemental analysis was obtained with a Flash EA 1112 elemental analyzer. <sup>1</sup>H NMR spectra were obtained with a 400 MHz Jeol ECA spectrometer. TGA data was collected with a ramp rate of 10 °C/min using a Rigaku TG8120 in flowing nitrogen. FT-IR spectra were collected using a Nicolet iD5 diamond ATR. Laboratory powder X-ray diffraction (PXRD) data were collected at ambient temperature on a Rigaku SmartLab X-ray diffractometer at 40 kV, 40 mA with Cu K $\alpha$  radiation. Gas adsorption experiments were conducted between 77 K and ambient temperature using a Bel-max gas adsorption machine with adsorption temperatures maintained by a custom-made cryo apparatus from BEL, Inc. Samples of **1'** and **2** were activated at 120 °C overnight before gas adsorption measurements.

**Powder Synthesis of  $\Delta$ DMF.** In an argon-filled MBraun glovebox, 37.5 mg of anhydrous MnCl<sub>2</sub> (Aldrich), 99.69 mg of H<sub>2</sub>bdc (TCI), and 328 mg of dpe (Aldrich) were added to a 50 mL glass bottle. The bottle was then filled with 30 mL of anhydrous DMF/methanol (80/20 v/v) (Wako) and sealed with a Teflon lined cap. The bottle was then brought out of the glovebox and heated at 120 °C for 24 h. The bright yellow powder was then filtered in air and washed with DMF and dried under vacuum. Weight of product = 0.140 g, and yield is quantitative with respect to Mn. Elemental analysis calculated for MnC<sub>23</sub>H<sub>21</sub>N<sub>3</sub>O<sub>5</sub>: C, 58.23; H, 4.46; N, 8.86. Found: C, 57.55; H, 4.44; N, 8.59.

**Powder Synthesis of **1'**.**  $\Delta$ DMF was heated at 180 °C for 5 h under dynamic vacuum to afford **1'**. It is stable and can be stored under ambient conditions. Elemental analysis calculated for MnC<sub>20</sub>H<sub>14</sub>N<sub>2</sub>O<sub>4</sub>: C, 59.86; H, 3.52; N, 6.98. Found: C, 60.61; H, 3.67; N, 7.04.

**Single Crystals of  $\Delta$ DMF.** A volume of 0.5 mL of MnClO<sub>4</sub> solution in DMF (40 mM) was added to 0.5 mL of H<sub>2</sub>bdc in DMF (40 mM) in a glass tube 0.3 cm in diameter. A buffer layer (0.5 mL) of DMF/MeOH (80/20 v/v) was then added carefully. Subsequently, 1 mL of dpe in MeOH (20 mM) was slowly added. The tube was then capped with a polypropylene cap and placed in an 80 °C oil-bath overnight. Yellow prism shaped crystals was observed and harvested by filtration and washing with DMF (see Table 1).

Table 1. Crystal Structure Data of  $\Delta$ DMF and **1'**

	$\Delta$ DMF	<b>1'</b>
Empirical formula	C <sub>43</sub> H <sub>35</sub> N <sub>5</sub> O <sub>9</sub> Mn <sub>2</sub>	C <sub>20</sub> H <sub>14</sub> N <sub>2</sub> O <sub>4</sub> Mn
Temperature (K)	223	223
Crystal system	Triclinic	Triclinic
Space group	P $\bar{1}$ (No. 2)	P $\bar{1}$ (No. 2)
<i>a</i> (Å)	10.0441(15)	9.2964(63)
<i>b</i> (Å)	10.5253(16)	10.1878(65)
<i>c</i> (Å)	11.3491(15)	12.0336(79)
<i>V</i> (Å <sup>3</sup> )	1051.1(3)	993.3(11)
$\alpha$ (°)	78.453(8)	95.769(93)
$\beta$ (°)	71.594(8)	99.637(32)
$\gamma$ (°)	68.025(8)	115.6732(8)
<i>Z</i>	1	2
<i>D</i> <sub>cal</sub> (g/cm <sup>3</sup> )	1.383	1.342
$\mu$ (mm <sup>-1</sup> )	0.66	0.69
Total reflections corrected	5489	7475
Reflections unique	3504	3994
Restraints/parameters	0/344	0/244
GoF on <i>F</i> <sup>2</sup>	1.256	1.225
<i>R</i> <sub>1</sub> indices [ <i>I</i> > 2 $\sigma$ ( <i>I</i> )]	0.1105	0.0581
<i>R</i> <sub>1</sub> indices (all data)	0.1126	0.0678
w <i>R</i> <sub>2</sub> (all data)	0.2503	0.1759

**Photodimerization of **1'** Affording **2**.** Approximately 6 mg of **1'** in powder form was placed between two glass microscopic slides and these were taped shut. The slides were then placed in a Luz-Chem photoreactor with top and side lamps and irradiated with UV radiation ( $\lambda_{max}$  = 350 nm). After 24 h, the slides were flipped for irradiation of the opposite side. The slides were then untaped, and the powder was manually mixed with a spatula. Three such flipping and mixing cycles were performed to afford a yellowish-white powder **2**. Elemental analysis calculated for MnC<sub>20</sub>H<sub>16</sub>N<sub>2</sub>O<sub>5</sub>: C, 57.29; H, 3.85; N, 6.68. Found: C, 56.75; H, 3.87; N, 6.60.

**Digestion of PCPs for Solution <sup>1</sup>H NMR.** One milligram of  $\Delta$ DMF, **1'**, or **2** was dissolved in 2 mL of 10% aqueous Na<sub>4</sub>EDTA (Aldrich) solution with the aid of sonication, followed by extraction (3 times) with 1 mL of CH<sub>2</sub>Cl<sub>2</sub> (Wako) in a 5 mL glass vial. The combined CH<sub>2</sub>Cl<sub>2</sub> extracts were evacuated, and the resulting white solid was dissolved in CD<sub>2</sub>Cl<sub>2</sub>.

**Single Crystal X-ray Diffraction (XRD) Measurements.** Measurements of  $\Delta$ DMF and **1'** were performed at 223 K with a Rigaku AFC10 diffractometer with Rigaku Saturn Kappa CCD system equipped with a MicroMax-007 HF/VariMax rotating-anode X-ray generator with confocal monochromated Mo K $\alpha$  radiation. The crystal structure was solved by a direct method and refined by full matrix least-squares refinement using Superflip<sup>13</sup> for  $\Delta$ DMF and SHELXL-97<sup>14</sup> for **1'**. The hydrogen atoms were added via a riding model. For  $\Delta$ DMF, the crystal is a non-merohedral twin.

**Synchrotron Powder XRD.** Synchrotron powder XRD measurements were performed at SPring-8 (Hyogo, Japan) BL44B2 beamline with  $\lambda$  = 0.80046 Å. For in situ gas adsorption measurements, a sample

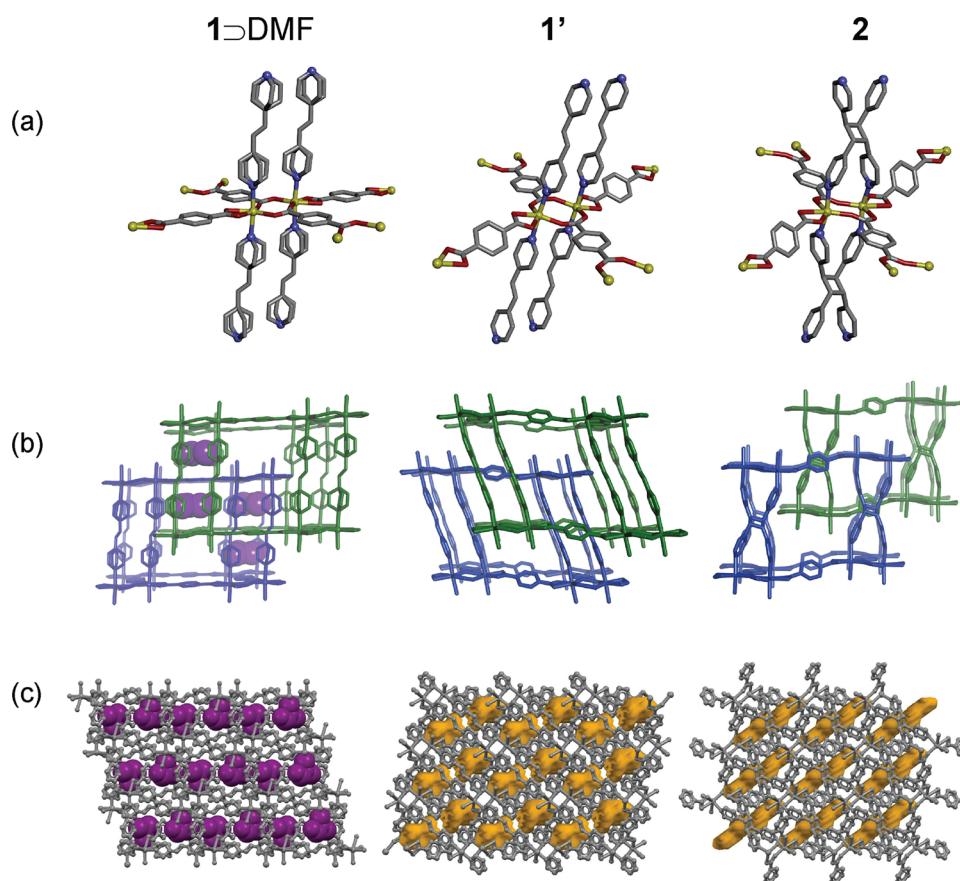


**Figure 1.** Crystal structures of 1⊃DMF (left), 1' (center), 2 (right) with hydrogens omitted for clarity. (a) Coordination environment of Mn. For 1⊃DMF, disordering in the pyridyl rings of dpe is present. Atoms are represented by colored spheres or sticks as Mn (yellow), O (red), N (blue), C (gray). (b) Box structural motif of 1⊃DMF, 1', 2 with emphasis on the two-fold interpenetrated structure represented by blue and green. DMF molecules in 1⊃DMF are represented by purple spheres. (c) The 3 × 3 × 3 unit cell emphasizing guest DMF molecules (purple spheres) for 1⊃DMF and void volume (probe radius 1.2 Å) for 1' and 2. Void space are visualized using Mercury CSD 2.0.<sup>18</sup>

of 1' was loaded into an open 0.4 mm glass capillary which was then connected to a custom-made gas-dosing apparatus (BEL Japan, Inc.). Synchrotron powder XRD of 1' and 2 at ambient was performed with a sealed 0.4 mm glass capillary.

**In Situ Gas Adsorption–PXRD.** In situ gas adsorption–PXRD measurements were carried out using a Rigaku SmartLab instrument with Cu K $\alpha$  radiation connected to a BELSORP-18PLUS volumetric adsorption equipment (BEL Japan, Inc.). The apparatuses were automated and synchronized with each other, and each X-ray diffraction pattern was obtained at each equilibrium point in the adsorption isotherm.

**Theoretical Calculations.** To find the most favorable interactive site of CO<sub>2</sub> or C<sub>2</sub>H<sub>2</sub> with the pore surface of 1', we evaluated the interaction energies between phenyl rings and CO<sub>2</sub> or C<sub>2</sub>H<sub>2</sub> in various symmetrical configurations. The obtained energetically most favorable structures were employed as initial structures for optimization without symmetric restriction. All geometry optimizations were carried out using density functional theory (DFT) method with B3LYP functional<sup>15</sup> augmented with the Grimme's D<sub>3</sub> correction<sup>16</sup> for dispersion interaction. Basis set of cc-pVTZ was used for all atoms. Interaction energies were evaluated by MP2 and the same basis set with BSSE correction. All calculations were carried out with the Gaussian 09 program package.<sup>17</sup>

## RESULTS AND DISCUSSION

The synthesis of microcrystalline powders of 1⊃DMF was achieved via solvothermal synthesis. Single crystals were obtained by layering of DMF and methanol solutions with a mixed DMF/MeOH buffer layer in-between. From single

crystal X-ray structural analysis, the asymmetric unit of 1⊃DMF consists of one Mn<sup>2+</sup> cation, one fully deprotonated bdc molecule, one disordered dpe molecule, and one DMF molecule. The formula of guest DMF was further verified by thermal gravimetric analysis (TGA), IR spectroscopy, and elemental analysis (Figures S1–S3). From TGA, 1⊃DMF is thermally stable until 380 °C in flowing N<sub>2</sub>. In the structure of 1⊃DMF (Figure 1), Mn is located in a distorted octahedral environment, in the axial position; it is coordinated by two nitrogen atoms from dpe ligands, and in the equatorial position, it is coordinated by two oxygen atoms from one bdc in chelating mode and two other oxygen atoms from two different bdc in monodentate mode. The two bdc ligands link two Mn ions with  $\mu$ -carboxylato fashion forming a Mn dimer cluster. The bond distances of the two crystallographically different Mn–N bonds are equivalent at 2.269 Å. The bond distances in Mn–O vary between 2.092 and 2.305 Å. The overall structure of 1⊃DMF has a 2-fold interpenetrated box motif with  $\alpha$ -Po topology. Each individual box motif consists of four Mn dimer clusters at each corner with Mn–Mn distances of 4.538 Å (Figure 1b). It is noted that the structure of 1⊃DMF is similar to that of previously reported [Zn(bdc)(dpe)].<sup>19</sup> However, for this PCP, the binuclear Zn cluster is rotated by 90° at every other corner, whereas 1⊃DMF has the same orientation throughout the crystal structure. 1⊃DMF appears to have undulating 1-D channels along the [011] direction; however, the continuity of the 1-D channels is disrupted by the edges of

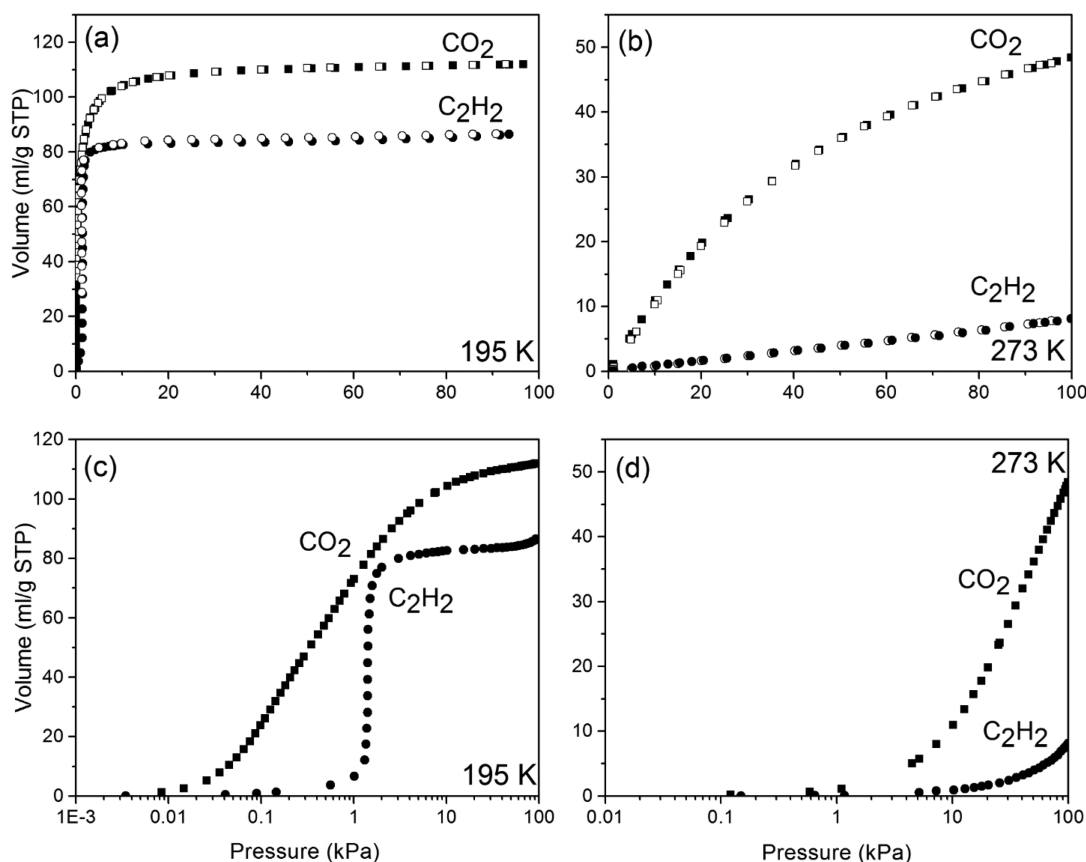


**Figure 2.** Sorption isotherms of **1'** for CO<sub>2</sub> and C<sub>2</sub>H<sub>2</sub>. The isotherms are measured at (a and c) 195 and (b and d) 273 K; (a and b) presented with linear abscissae; (c and d) shown in logarithmic abscissae. Circles and squares represent C<sub>2</sub>H<sub>2</sub> and CO<sub>2</sub>, respectively. Close and open symbols represent adsorption and desorption, respectively.

the pyridyl rings from dpe resulting in the formation of isolated 0-D pores that are filled by one DMF molecule each (Figure 1c). It is noted that each DMF molecule is sandwiched between two phenylene rings from bdc with orthogonal orientation of the carboxylate group (Figure S4). The rings are almost eclipsed with distances from the centroid of each benzene ring to DMF (N–C<sub>carbonyl</sub>) of 3.488 and 3.439 Å, respectively; this implies significant  $\pi$ – $\pi$  interactions between the two phenylene rings and DMF. After solvent removal with heating under vacuum to afford **1'** (Figure 1), the structure undergoes distortion via shearing of the box structural motif with concurrent tilting of the dpe pillars (24°) and significant rotation of the phenylene ring of bdc with chelating mode (25° with respect to the mean plane defined by the four carboxylate oxygens). This rotation of the aromatic ring is the most important change because the tilted rings further reduced the volume of 0-D pore, resulting in the formation of dimers of kidney-shaped isolated porous structure (each with dimensions of approximately 3.3 × 3.5 × 5.6 Å<sup>3</sup>) along the [10 $\bar{1}$ ] direction. Each 0-D pore is separated from each other due to the tilted rings from bdc and dpe. Thus, the pore system can be considered as undulating pseudo 1-D channels assembled by 0-D pores. The unit cell volume is reduced from the original as-synthesized 1051 to 993 Å<sup>3</sup>. From Platon program, the void volume is calculated to be 17.4% (173 Å<sup>3</sup>).

The gas adsorption properties of **1'** were studied with respect to N<sub>2</sub> at 77 K, O<sub>2</sub>, CO<sub>2</sub> and CH<sub>4</sub> at 195 K using a crystalline powder sample (Figure S5). For O<sub>2</sub>, N<sub>2</sub>, and CH<sub>4</sub>, no appreciable adsorption could be observed due to the non-

porosity of the pseudo-1-D channels for these gas molecules. However, **1'** adsorbs 111 mL (STP)/g (1.97 mmol CO<sub>2</sub>/mmol Mn or 21.6 wt %) of CO<sub>2</sub> at 195 K, which may be due to its smallest kinetic diameter (3.3 Å) enabling the access of CO<sub>2</sub> into the pseudo-1-D channels. It is noted that there are approximately 4 molecules of CO<sub>2</sub> per unit cell ( $Z = 2$ ), in good agreement with the void volume of **1**. As **1'** does not adsorb N<sub>2</sub> at 77 and 195 K (Figures S5 and S6), its surface area was calculated by CO<sub>2</sub> adsorption at 195 K using the Brunauer–Emmett–Teller (BET) model to afford a surface area of 535 m<sup>2</sup>/g (Figure S7). The isosteric heat of adsorption,  $Q_{st}$  for CO<sub>2</sub> is calculated by the virial method to be 29–30 kJ/mol and does not change appreciably with loading (Figure S8), suggesting uniformity of binding sites. In addition, the  $Q_{st}$  for CO<sub>2</sub> of our compound is moderately high compared to MOFs with no open metal sites or polar functional groups such as MOF-508 [Zn(bdc)(bpy)<sub>0.5</sub>]<sup>20</sup> (with  $Q_{st}$  of 16–20 kJ/mol).<sup>21</sup> From a practical standpoint, the constant and moderately high value of  $Q_{st}$  at different loadings renders **1'** useful for the effective separations of CO<sub>2</sub> from other gases. The adsorption isotherm of C<sub>2</sub>H<sub>2</sub> was obtained at 195 K (Figure 2a,c). Unlike the CO<sub>2</sub> case, a gated behavior (with  $P_{go} = 1.45$  kPa) was clearly observed. Below the gate opening pressure, adsorption of C<sub>2</sub>H<sub>2</sub> is negligible, but an abrupt increase is observed after  $P_{go}$  reaches 86.2 mL/g STP (1.55 mmol C<sub>2</sub>H<sub>2</sub>/mmol Mn). In sharp contrast, for CO<sub>2</sub> the gas uptake is increasing monotonically and no clear gate opening behavior was observed even at low pressure region. This behavior is markedly different from other 0-D frameworks such as

[Cu(etz)] (hetz = 3,5-diethyl-1,2,4-triazole) where gate opening pressures is observed for both CO<sub>2</sub> and C<sub>2</sub>H<sub>2</sub>.<sup>22</sup>

On increasing the adsorption temperature to 273 K (Figure 2b,d), for 1',  $P_{go}$  for C<sub>2</sub>H<sub>2</sub> adsorption increases to greater than 1 atm; thus, adsorption (91 kPa, 7.3 mL/g STP) is negligible with linear adsorption profile, resulting in low heats of adsorption (Figure S9). In contrast, CO<sub>2</sub> is adsorbed smoothly even at 273 K (46.8 mL/g STP at 91 kPa) without gate opening behavior despite the considerably narrow paths in the pseudo-1-D channels.

The ratio of CO<sub>2</sub>/C<sub>2</sub>H<sub>2</sub> adsorbed at 90 kPa is 6.4, which suggests that 1' is potentially useful for separating CO<sub>2</sub> from C<sub>2</sub>H<sub>2</sub> with high selectivity at noncryogenic temperatures. It is noted that this ratio is the highest achieved until date for inverse selectivity of CO<sub>2</sub>/C<sub>2</sub>H<sub>2</sub> near room temperature (Table S2). To establish the feasibility of gas separations, the ideal adsorbed solution theory (IAST) calculations<sup>23</sup> were used to predict the separation of an equimolar amount of C<sub>2</sub>H<sub>2</sub> and CO<sub>2</sub> from its pure isotherms at 273 K (Figure S10). The CO<sub>2</sub>/C<sub>2</sub>H<sub>2</sub> selectivity for an equimolar CO<sub>2</sub>/C<sub>2</sub>H<sub>2</sub> gas mixture varies from 8.8 to 13. The results from the IAST calculations indicate that 1' may be suitable for practical use as a material for separating CO<sub>2</sub> from a CO<sub>2</sub>/C<sub>2</sub>H<sub>2</sub> mixture over a wide range of pressures at ambient temperature.

To evaluate the gas separation ability of adsorbents under kinetic gas conditions, breakthrough simulations were performed,<sup>24</sup> which are strongly pertinent to the pressure swing adsorption (PSA) process, an energetically efficient method for industrial scale separations. With the aid of transient breakthrough simulations, we aim to demonstrate that pure C<sub>2</sub>H<sub>2</sub> can be produced during the adsorption phase in fixed-bed adsorbents. The performance of industrial fixed bed adsorbents is dictated by a combination of adsorption selectivity and working capacity. The breakthrough simulations were performed for a total gas pressure of 100 kPa, and constant temperature of 273 K. The transient breakthrough simulation results are presented in terms of a dimensionless time,  $\tau$ , which is a metric determining the frequency of required regeneration and influencing the productivity of a PSA unit. Figure 3a presents the results for a 50/50 CO<sub>2</sub>/C<sub>2</sub>H<sub>2</sub> mixture. The y-axis in Figure 3a is the dimensionless concentration of each component normalized with respect to the concentration at the feed inlet concentration. We note that the separation is very sharp with the breakthrough curves for CO<sub>2</sub> and C<sub>2</sub>H<sub>2</sub> showing near-vertical slopes. As C<sub>2</sub>H<sub>2</sub> possesses low affinity to 1', it breaks through quickly and  $\tau$  for CO<sub>2</sub> to break through is  $\sim 7$ –8 times longer. The ability of 1' to selectively adsorb CO<sub>2</sub> is an important advantage of this flexible PCP/MOF as pure C<sub>2</sub>H<sub>2</sub> can be produced during the “adsorption” phase of fixed-bed adsorption operations. Other PCPs/MOFs have been suggested in the literature as being suitable for separation of CO<sub>2</sub>/C<sub>2</sub>H<sub>2</sub> mixtures: (1) HOF-3 (a rod-packing 3D microporous hydrogen-bonded organic framework),<sup>25</sup> (2) HKUST-1 (= Cu<sub>3</sub>(BTC))<sub>2</sub>,<sup>26</sup> (3) ZJU-60a (= Cu<sub>2</sub>(MFDI)),<sup>27</sup> (4) PCP-33,<sup>28</sup> and (5) MIL-100 (Fe).<sup>29</sup> All five of these PCPs/MOFs adsorb C<sub>2</sub>H<sub>2</sub> selectively. As a consequence, pure C<sub>2</sub>H<sub>2</sub> can only be produced in the “desorption” phase of fixed bed adsorbent operations with these PCPs/MOFs. The attainment of high purity product in the desorption phase is considerably more difficult in fixed bed operations compared to obtaining the product via the adsorption phase.<sup>30</sup>

It is noted that for flexible PCPs/MOFs, despite some recent works,<sup>31</sup> there remains some controversy about their ability to

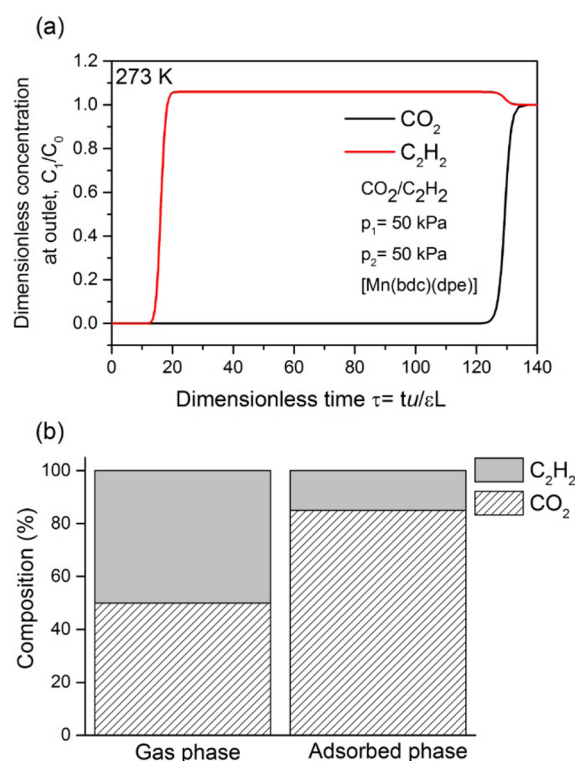


**Figure 3.** (a) Simulated breakthrough curve at 273 K for a 50/50 mixture of CO<sub>2</sub>/C<sub>2</sub>H<sub>2</sub> at 100 kPa. (b) Gas separation experiment results obtained by flowing 50/50 mixture of CO<sub>2</sub>/C<sub>2</sub>H<sub>2</sub> at 273 K, followed by ascertaining composition of adsorbed phase by gas chromatography.

separate mixtures since it can be reasoned that on adsorption of one component, the other component may be simultaneously adsorbed despite the appearance of their respective pure isotherms. To verify that 1' can indeed separate C<sub>2</sub>H<sub>2</sub> from a CO<sub>2</sub>/C<sub>2</sub>H<sub>2</sub> mixture, we have performed a trial gas separation experiment using a flowing 50/50 CO<sub>2</sub>/C<sub>2</sub>H<sub>2</sub> mixture at 100 kPa and 273 K. The results of the experiment (Figure 3b, Figure S11) show that CO<sub>2</sub> is selectively adsorbed from CO<sub>2</sub>/C<sub>2</sub>H<sub>2</sub> mixture as the gas composition of the adsorbed component is 85/15, whereas the flowing gas composition is 50/50. The partition coefficient is 5.7, which is greater than one, indicating that preferential adsorption of CO<sub>2</sub> does occur in the presence of C<sub>2</sub>H<sub>2</sub>.

To further understand temperature dependency of the adsorption behavior for CO<sub>2</sub> and C<sub>2</sub>H<sub>2</sub>, additional adsorption measurements were performed at different temperatures between 195 and 273 K. For C<sub>2</sub>H<sub>2</sub>, a steady increase in  $P_{go}$  with temperature is observed (Figure 4), consistent with previous observations in the literature.<sup>32</sup>

A linear plot is obtained by plotting the gate opening pressures vs inverse of temperature (Figure S12), similar to previous studies.<sup>33</sup> It is established that above 252 K, the gate opening pressure is larger than 100 kPa. For CO<sub>2</sub>, no clear gate opening pressure is observed at any temperature, suggesting that adsorption of CO<sub>2</sub> is smooth with no difficulty in the diffusion of CO<sub>2</sub> molecules in pseudo-1-D channels.

To elucidate the reason for the presence of  $P_{go}$  for C<sub>2</sub>H<sub>2</sub> but its absence in CO<sub>2</sub> adsorption, in situ adsorption coupled with X-ray diffraction experiments were performed (Figure 5).<sup>34</sup> Due to the triclinic symmetry and considerable overlap of peaks, complete indexing of the patterns could not be

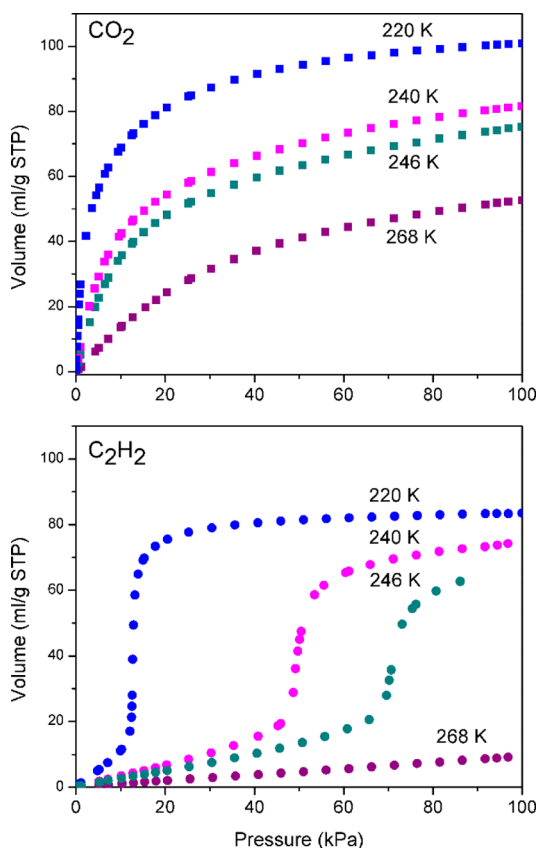


**Figure 4.** Adsorption isotherms of CO<sub>2</sub> (top) and C<sub>2</sub>H<sub>2</sub> (bottom) for I' at 220, 240, 246, and 268 K.

satisfactorily performed. However, significant difference in the X-ray diffraction patterns could be observed upon adsorption between CO<sub>2</sub> and C<sub>2</sub>H<sub>2</sub>. In the case of CO<sub>2</sub> adsorption, a continuous shift of peaks, especially for the two peaks indexed as (002) and (11 $\bar{1}$ ) to lower angle region in the PXRD patterns, was seen, suggesting that the framework expands gradually in response to the increasing volume of CO<sub>2</sub> adsorbed. On the other hand, the in situ PXRD patterns for C<sub>2</sub>H<sub>2</sub> show two main phases,  $\alpha$  and  $\beta$ , which correspond to the closed phase before gate opening and the open form after gate opening, respectively. From Figure 5, it is evident that along the sharp vertical adsorption step (Figure 5, points B and C in the isotherm of C<sub>2</sub>H<sub>2</sub>), both  $\alpha$  and  $\beta$  phases are present and their relative proportions (as elucidated by the intensity of the powder diffraction peaks) are in good agreement with the relative amount adsorbed.

In addition, attempts were made to obtain the lattice parameters of the gas-filled phases of **2** at 195 K via synchrotron radiation. For 1 $\Delta$ CO<sub>2</sub>, a good Le Bail fit (Figure S13a) could be performed. The following lattice parameters were obtained:  $a = 9.6609(3)$  Å,  $b = 11.5232(4)$  Å,  $c = 10.5314(2)$  Å;  $\alpha = 105.684(3)^\circ$ ,  $\beta = 114.898(2)^\circ$ ,  $\gamma = 81.211(2)^\circ$ . The unit cell volume is 1023 Å<sup>3</sup>, which is clearly larger than that of dried I' (993 Å<sup>3</sup>), consistent with occupation by gas molecules. However, for 1 $\Delta$ C<sub>2</sub>H<sub>2</sub>, the indexing was not very successful due to the complex PXRD pattern. Despite this limitation, the appearance of low angle peaks and the best indexing result (Figure S13b) suggests a much larger unit cell volume was obtained compared to 1 $\Delta$ CO<sub>2</sub>, which implies a much larger structural change has occurred with approximately the same volume of gas adsorbed.

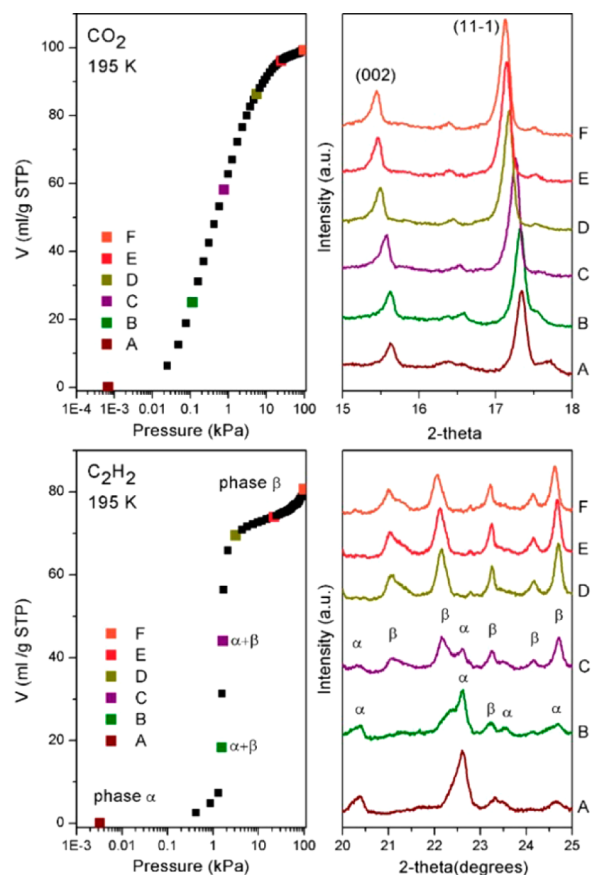


**Figure 5.** Adsorption isotherms and in situ adsorption-XRD of I' for CO<sub>2</sub> at 195 K (top) and C<sub>2</sub>H<sub>2</sub> at 195 K (bottom).

Once again, this unusual large difference in adsorption between CO<sub>2</sub> and C<sub>2</sub>H<sub>2</sub> is unprecedented. As mentioned above, CO<sub>2</sub> and C<sub>2</sub>H<sub>2</sub> have very similar size and physicochemical properties, but they possess opposite quadrupole moment around rod shaped bodies. Therefore, to understand the large difference in gas adsorption for these two gases, we initially assumed that I' should recognize the opposite quadrupole moment of these two molecules. On the other hand, I' has very small pores which can be classified as almost 0-D, as is described above. Both molecules cannot diffuse into the channels if we consider these gas molecules as rigid sphere model with kinetic diameters of 3.3 Å. However, they have rod-shaped anisotropic molecular dimensions. Hence, if the molecule thrusts into the pore in an end-on type fashion (principle axis along the channel direction), the minimum accessible size of pore should be much less than that of kinetic diameter, which may possibly allow CO<sub>2</sub> and C<sub>2</sub>H<sub>2</sub> molecules to diffuse into such small pores. As the pores of I' are quite small, its crystallographic structure suggests that the molecules cannot move around freely in the pore but are forced to keep its orientation during diffusion and adsorption unless a structural expansion occurs.

Consequently, our hypothesis of inverse adsorption selectivity is shown in Figure 6: the electrostatic potential formed in the small pore effectively interacts with the quadrupole moment of CO<sub>2</sub> in an end-on orientation along the channel direction, resulting in the gradual and smooth adsorption (I, II) with a gradual change in cell parameters. On the other hand, the pore potential results in repulsive interaction with C<sub>2</sub>H<sub>2</sub> in an end-on orientation because of the opposite quadrupole

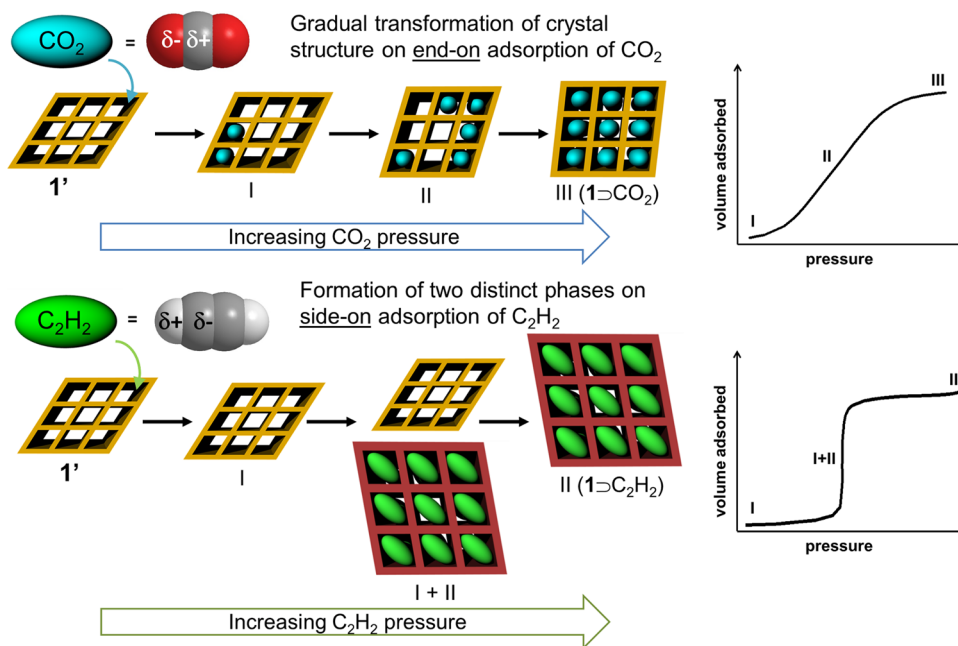


**Figure 6.** Possible adsorption mechanism of 1' for CO<sub>2</sub> (top, gradual transformation) and C<sub>2</sub>H<sub>2</sub> (bottom, two-phase gated adsorption) at 195 K with corresponding adsorption isotherms. Note that the unit cell volume of 1-C<sub>2</sub>H<sub>2</sub> is much larger than that of 1-CO<sub>2</sub> as revealed by in situ synchrotron X-ray diffraction.

moment, thus refusing access to C<sub>2</sub>H<sub>2</sub> in the low pressure region (below  $P_{go}$  (I)) and requires large structural transformation to adsorb C<sub>2</sub>H<sub>2</sub> with side-on orientation (principle axis perpendicular to the channel direction).

To prove our hypothesis, we first conducted DFT calculations whereupon a CO<sub>2</sub> or C<sub>2</sub>H<sub>2</sub> molecule is inserted between two phenyl rings initially 6.924 Å apart, which is experimentally observed in 1-DMF. The geometries are optimized by keeping the two phenyl rings in parallel. For CO<sub>2</sub>, the distance shrinks to 6.575 Å with the most stable molecular configuration that CO<sub>2</sub> molecules are parallel to phenylene rings (i.e., keeping end-on access fashion). For C<sub>2</sub>H<sub>2</sub>, the most stable configuration is perpendicular to phenylene rings to maximize electrostatic interaction (CH- $\pi$  interactions in this case), which requires pore expansion making the distance between phenylene rings 8.324 Å (Figure 7). This is consistent with our hypothesis that CO<sub>2</sub> tends to migrate into pores more smoothly, whereas C<sub>2</sub>H<sub>2</sub> is refused without the occurrence of gate opening behavior.

Second, we obtained experimental evidence further supporting our proposed mechanism. As elucidated in the DFT calculation, the local flexibility of the phenylene rings plays an

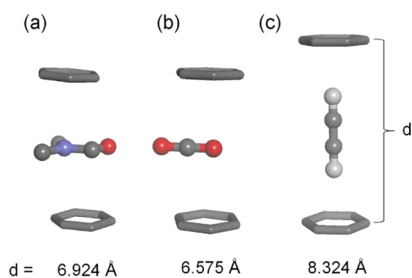


**Figure 7.** Distance between the centroids of two stacked benzene rings (a) as experimentally observed in 1-DMF. As optimized by DFT calculations for (b) CO<sub>2</sub> and (c) C<sub>2</sub>H<sub>2</sub>.

important role in the adsorption event. We expect that if we could induce changes in the orientation of the phenyl rings in 1', such as tilting against channel direction, effective interaction between the phenylene plane and guest molecules is rendered highly impossible, which could result in destroying the adsorption selectivity.

To realize such structural change, we attempted [2 + 2] photodimerization of the dpe ligands to ascertain its effect on the conformation of phenyl rings. This is due to two reasons: First, the dpe pillars seem to be key for structural flexibility due to differences of the tilt angle in 1 and 1'. Second, [2 + 2] photodimerization is highly feasible because the ethylenic carbons in 1' at each corner of the box motif are eclipsed at a distance of 4.024 Å apart, which fulfills Schimidt's criterion<sup>35</sup> (<4.2 Å).

After exposing 1' to UV ( $\lambda_{max} = 350$  nm) irradiation for 1 week, powders of 1' changed significantly from bright yellow to whitish-yellow (Figure S14). In comparison to Zn coordination polymers, [2 + 2] photodimerization of Mn coordination polymers is relatively rare.<sup>36</sup> The color change strongly suggests that the conjugation of Mn-dpe-Mn system has been lost via photodimerization. Digestion of the photoirradiated product followed by <sup>1</sup>H NMR and mass spectrometry (Figures S15 and S16) verified the quantitative dimerization to tetrakis(4-pyridyl)cyclobutane (tpcb) by the complete disappearance of the olefin protons at  $\delta = 7.25$  ppm and shifting of the two pyridyl protons with peaks centered at  $\delta = 7.43, 8.60$  ppm. It is noted that only one set of cyclobutane protons is observed at  $\delta = 4.48$  ppm. Thus, the [2 + 2] photodimerization is completely regioselective as only the *rcct* isomer is present.<sup>37</sup> Hence, 1' has undergone [2 + 2] photodimerization to form 2 (Figure 8). From TGA (Figure S17), the thermal stability of 2 did not differ appreciably from that of 1'.

Because of severe deterioration of single crystallinity upon the photodimerization from 1' to 2, structural determination of the photodimerized compound 2 was unsuccessful. However,

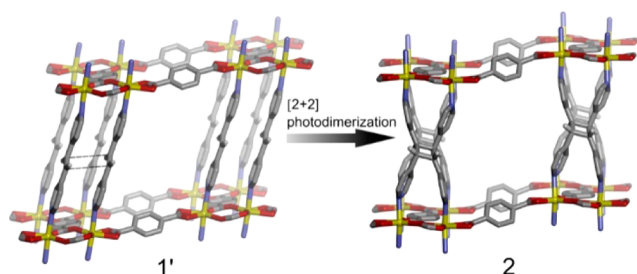


**Figure 8.** Transformation of **1'** into **2** via [2 + 2] photodimerization of the coordinated dpe ligands. For simplicity, the two-fold interpenetration in the both structures is neglected and only a single box motif is considered. Aromatic protons are excluded for clarity. The dotted lines in **1'** indicate the eclipsed C=C bonds with distances of 4.024 Å.

we could successfully obtain the crystal structure of **2** from performing a Rietveld analysis with high reliability ( $R_{wp}$  of 3.64%) on a high quality synchrotron XRD pattern (Figures S18 and S19) using a preliminary dimerized structure optimized with molecular mechanics<sup>38</sup> from the structure of **2** (Figure 1); it is observed that the unit cell volume of **2** is slightly reduced from 993 to 981 Å<sup>3</sup>. Due to the pyridyl rings displacing closer to each other for the dimerization to occur, the nearly linear Mn–N–Mn bond angle is distorted from 177° in **1'** to 164° in **2**. In addition, the Mn–Mn distance is now lengthened to 4.287 Å. Interestingly, the tilt of the bdc phenyl rings in the chelating mode is also significantly increased from the original 25 to 45°.

Although the porosity of **2** is almost similar to that of **1'** (17.5%, 172 Å<sup>3</sup>), which was also confirmed by a Type I isotherm of O<sub>2</sub> at 90 K (Figure S20), now all adjacent 0-D kidney-shaped pores are merged and flattened to afford a single cigar-shaped pore of 2.7 × 3.4 × 13.5 Å<sup>3</sup>. Interestingly, in the CO<sub>2</sub> gas adsorption isotherm at 273 K for **2** (Figure 9), it is

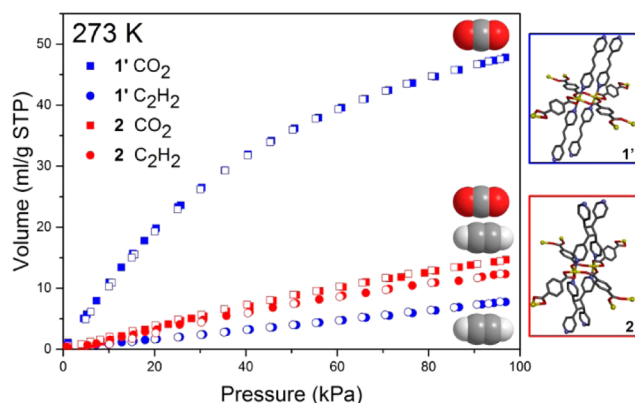


**Figure 9.** Gas sorption isotherms for CO<sub>2</sub> and C<sub>2</sub>H<sub>2</sub> for **1'** (blue) and **2** (red) at 273 K. Squares represent CO<sub>2</sub> and circles C<sub>2</sub>H<sub>2</sub>. Open symbols represent adsorption and closed symbols desorption.

observed that its profile is linear with a significant decrease in uptake compared to the case for **1'**. In addition, the uptake of CO<sub>2</sub> (14.1 mL/g STP) and C<sub>2</sub>H<sub>2</sub> (11.8 mL/g STP) at 91 kPa for **2** is now almost identical. This indicates that after photodimerization, in the pores of the resultant PCP, CO<sub>2</sub> molecules cannot interact with phenylene rings efficiently because of the significant tilting of phenylene rings upon photodimerization, resulting in the loss of its inverse selectivity

for CO<sub>2</sub>/C<sub>2</sub>H<sub>2</sub> and its sorption behavior. It is noted that the ethylenic double bonds in **1'** are not lining the pore surface; thus, they are not contributing to adsorption selectivity. This result strongly supports the proposed mechanism of the inversed selectivity in **1'** based on the guest discriminatory gated effect.

## CONCLUSIONS

In conclusion, we have demonstrated an alternative concept for separating gases with similar size and physical properties. In contrast to conventional approaches such as strong chemical interactions and/or molecular sieving, our approach entails selecting a soft framework with narrow 0-D pores, which will selectively exhibit gate opening behavior for one of the components due to differences in electronic properties. For such an approach to work, the pores must be narrow leading to the gas molecules possessing intimate contact with the pore environment. In addition, the gas molecules should possess distinctly different electronic properties, i.e., CO<sub>2</sub> and C<sub>2</sub>H<sub>2</sub> have quadrupole moment of different signs resulting in (thus requiring) different distortions of the pore environment. It is noted that in this instance, both global (change in crystal structure) and local (tilt in phenylene ring of bdc) flexibility are important for showing the selective gate opening behavior for C<sub>2</sub>H<sub>2</sub>.

As the gate opening pressure increases with temperature, the selectivity of separation will increase with increasing temperature. This is seen in the sorption behavior of **1'** and leads to the clear manifestation of inverse selectivity—the preferential adsorption of CO<sub>2</sub> over C<sub>2</sub>H<sub>2</sub> at 273 K. As refrigeration is both expensive and energy intensive, separations close to ambient temperatures will be increasingly important for industrial applications. We have demonstrated the feasibility of this with a preliminary gas separation experiment under flowing conditions using a 50/50 CO<sub>2</sub>/C<sub>2</sub>H<sub>2</sub> gas mixture.

## ASSOCIATED CONTENT

### Supporting Information

The Supporting Information is available free of charge on the ACS Publications website at DOI: 10.1021/jacs.5b10491.

<sup>1</sup>H NMR, XRD, TGA, IR of **1**, **1'** and **2** (PDF)

X-ray crystallographic file of **1** (CCDC 1008212), **1'** (CCDC 1008213), and **2** (CCDC 1048123) (CIF)

Movie with further information on the breakthrough simulation for 50/50 CO<sub>2</sub>/C<sub>2</sub>H<sub>2</sub> gas mixture at 100 kPa (MPG)

## AUTHOR INFORMATION

### Corresponding Authors

\*ryotaro.matsuda@apchem.nagoya-u.ac.jp

\*kitagawa@icems.kyoto-u.ac.jp

### Present Address

<sup>†</sup>National University of Singapore, Department of Chemistry, 3 Science Drive 3, Singapore 117543.

### Notes

The authors declare no competing financial interest.

## ACKNOWLEDGMENTS

We thank Dr. Hiroyasu Sato from Rigaku Corporation, Japan for his assistance in solving the crystal structure of **1**. T. Nishijima and T. Fuke provided expert technical support. This



work is supported by the PRESTO and ACCEL project of the Japan Science and Technology Agency (JST), and JSPS KAKENHI Grant-in-Aid for Young Scientists (B) (Grant No. 25870360), for Challenging Exploratory Research (Grant No. 25620187) and for Specially Promoted Research (Grant No. 25000007). This work was also supported in part by the New Energy and Industrial Technology Development Organization (NEDO). iCeMS and ITbM is supported by the World Premier International Research Initiative (WPI) of the Ministry of Education, Culture, Sports, Science and Technology, Japan (MEXT).

## REFERENCES

- (1) (a) Pässler, P.; Hefner, W.; Buckl, K.; Meinass, H.; Meiswinkel, A.; Wernicke, H.-J.; Ebersberg, G.; Müller, R.; Bäessler, J.; Behringer, H.; Mayer, D. *Ullmann's Encyclopedia of Industrial Chemistry*; Wiley-VCH Verlag GmbH & Co. KGaA, 2000. (b) Gannon, R. E. *Kirk-Othmer Encyclopedia of Chemical Technology*; John Wiley & Sons, Inc., 2000.
- (2) Matsuda, R.; Kitaura, R.; Kitagawa, S.; Kubota, Y.; Belosludov, R. V.; Kobayashi, T. C.; Sakamoto, H.; Chiba, T.; Takata, M.; Kawazoe, Y.; Mita, Y. *Nature* **2005**, *436*, 238.
- (3) Yang, W.; Davies, A. J.; Lin, X.; Suyetin, M.; Matsuda, R.; Blake, A. J.; Wilson, C.; Lewis, W.; Parker, J. E.; Tang, C. C.; George, M. W.; Hubberstey, P.; Kitagawa, S.; Sakamoto, H.; Bichoutskaia, E.; Champness, N. R.; Yang, S.; Schroder, M. *Chem. Sci.* **2012**, *3*, 2993.
- (4) Eguchi, R.; Uchida, S.; Mizuno, N. *Angew. Chem., Int. Ed.* **2012**, *51*, 1635.
- (5) (a) Kitagawa, S.; Kitaura, R.; Noro, S.-i. *Angew. Chem., Int. Ed.* **2004**, *43*, 2334. (b) Janiak, C.; Vieth, J. K. *New J. Chem.* **2010**, *34*, 2366. (c) Furukawa, H.; Cordova, K. E.; O'Keeffe, M.; Yaghi, O. M. *Science* **2013**, *341*, 1230444. (d) Rowsell, J. L. C.; Yaghi, O. M. *Microporous Mesoporous Mater.* **2004**, *73*, 3. (e) Li, J.-R.; Sculley, J.; Zhou, H.-C. *Chem. Rev.* **2012**, *112*, 869.
- (6) (a) Uemura, K.; Matsuda, R.; Kitagawa, S. *J. Solid State Chem.* **2005**, *178*, 2420. (b) Ferey, G.; Serre, C. *Chem. Soc. Rev.* **2009**, *38*, 1380. (c) Schneemann, A.; Bon, V.; Schwedler, L.; Senkovska, I.; Kaskel, S.; Fischer, R. A. *Chem. Soc. Rev.* **2014**, *43*, 6062.
- (7) Horike, S.; Shimomura, S.; Kitagawa, S. *Nat. Chem.* **2009**, *1*, 695.
- (8) Kitaura, R.; Seki, K.; Akiyama, G.; Kitagawa, S. *Angew. Chem., Int. Ed.* **2003**, *42*, 428. (b) Li, D.; Kaneko, K. *Chem. Phys. Lett.* **2001**, *335*, 50.
- (9) (a) Xiao, B.; Byrne, P. J.; Wheatley, P. S.; Wragg, D. S.; Zhao, X. B.; Fletcher, A. J.; Thomas, K. M.; Peters, L.; Evans, J. S. O.; Warren, J. E.; Zhou, W. Z.; Morris, R. E. *Nat. Chem.* **2009**, *1*, 289. (b) Henke, S.; Schneemann, A.; Wütscher, A.; Fischer, R. A. *J. Am. Chem. Soc.* **2012**, *134*, 9464.
- (10) Yanai, N.; Kitayama, K.; Hijikata, Y.; Sato, H.; Matsuda, R.; Kubota, Y.; Takata, M.; Mizuno, M.; Uemura, T.; Kitagawa, S. *Nat. Mater.* **2011**, *10*, 787.
- (11) (a) Ma, S.; Sun, D.; Wang, X.-S.; Zhou, H.-C. *Angew. Chem., Int. Ed.* **2007**, *46*, 2458. (b) Nijem, N.; Wu, H.; Canepa, P.; Martí, A.; Balkus, K. J.; Thonhauser, T.; Li, J.; Chabal, Y. J. *J. Am. Chem. Soc.* **2012**, *134*, 15201.
- (12) (a) Witte, J.; Neaton, J. B.; Head-Gordon, M. *J. Chem. Phys.* **2014**, *140*, 104707. (b) Majumder, M.; Mishra, B. K.; Sathyamurthy, N. *Chem. Phys. Lett.* **2013**, *557*, 59.
- (13) Oszlanyi, G.; Suto, A. *Acta Crystallogr., Sect. A: Found. Crystallogr.* **2005**, *61*, 147.
- (14) Sheldrick, G. *Acta Crystallogr., Sect. A: Found. Crystallogr.* **2008**, *64*, 112.
- (15) (a) Becke, A. D. *J. Chem. Phys.* **1993**, *98*, 5648. (b) Lee, C.; Yang, W.; Parr, R. G. *Phys. Rev. B: Condens. Matter Mater. Phys.* **1988**, *37*, 785.
- (16) Grimme, S.; Antony, J.; Ehrlich, S.; Krieg, H. *J. Chem. Phys.* **2010**, *132*, 154104.
- (17) Frisch, M. J.; Trucks, G. W.; Schlegel, H. B.; Scuseria, G. E.; Robb, M. A.; Cheeseman, J. R.; Scalmani, G.; Barone, V.; Mennucci, B.; Petersson, G. A.; Nakatsuji, H.; Caricato, M.; Li, X.; Hratchian, H. P.; Izmaylov, A. F.; Bloino, J.; Zheng, G.; Sonnenberg, J. L.; Hada, M.; Ehara, M.; Toyota, K.; Fukuda, R.; Hasegawa, J.; Ishida, M.; Nakajima, T.; Honda, Y.; Kitao, O.; Nakai, H.; Vreven, T.; Montgomery Jr., J. A.; Peralta, J. E.; Ogliaro, F.; Bearpark, M. J.; Heyd, J.; Brothers, E. N.; Kudin, K. N.; Staroverov, V. N.; Kobayashi, R.; Normand, J.; Raghavachari, K.; Rendell, A. P.; Burant, J. C.; Iyengar, S. S.; Tomasi, J.; Cossi, M.; Rega, N.; Millam, N. J.; Klene, M.; Knox, J. E.; Cross, J. B.; Bakken, V.; Adamo, C.; Jaramillo, J.; Gomperts, R.; Stratmann, R. E.; Yazyev, O.; Austin, A. J.; Cammi, R.; Pomelli, C.; Ochterski, J. W.; Martin, R. L.; Morokuma, K.; Zakrzewski, V. G.; Voth, G. A.; Salvador, P.; Dannenberg, J. J.; Dapprich, S.; Daniels, A. D.; Farkas, Ö.; Foresman, J. B.; Ortiz, J. V.; Cioslowski, J.; Fox, D. J. *Gaussian 09*; Gaussian, Inc.: Wallingford, CT, 2009.
- (18) Macrae, C. F.; Bruno, I. J.; Chisholm, J. A.; Edgington, P. R.; McCabe, P.; Pidcock, E.; Rodriguez-Monge, L.; Taylor, R.; van de Streek, J.; Wood, P. A. *J. Appl. Crystallogr.* **2008**, *41*, 466.
- (19) Mir, M. H.; Koh, L. L.; Tan, G. K.; Vittal, J. J. *Angew. Chem., Int. Ed.* **2010**, *49*, 390.
- (20) Chen, B.; Liang, C.; Yang, J.; Contreras, D. S.; Clancy, Y. L.; Lobkovsky, E. B.; Yaghi, O. M.; Dai, S. *Angew. Chem., Int. Ed.* **2006**, *45*, 1390.
- (21) Bastin, L.; Bácia, P. S.; Hurtado, E. J.; Silva, J. A. C.; Rodrigues, A. E.; Chen, B. *J. Phys. Chem. C* **2008**, *112*, 1575.
- (22) Zhang, J.-P.; Chen, X.-M. *J. Am. Chem. Soc.* **2009**, *131*, 5516.
- (23) (a) Myers, A. L.; Prausnitz, J. M. *AIChE J.* **1965**, *11*, 121. (b) Babarao, R.; Hu, Z.; Jiang, J.; Chempath, S.; Sandler, S. I. *Langmuir* **2007**, *23*, 659.
- (24) (a) Krishna, R. *Microporous Mesoporous Mater.* **2014**, *185*, 30. (b) Krishna, R. *RSC Adv.* **2015**, *5*, 52269.
- (25) Li, P.; He, Y.; Zhao, Y.; Weng, L.; Wang, H.; Krishna, R.; Wu, H.; Zhou, W.; O'Keeffe, M.; Han, Y.; Chen, B. *Angew. Chem., Int. Ed.* **2015**, *54*, 574.
- (26) Xiang, S.; Zhou, W.; Gallegos, J. M.; Liu, Y.; Chen, B. *J. Am. Chem. Soc.* **2009**, *131*, 12415.
- (27) Duan, X.; Zhang, Q.; Cai, J.; Yang, Y.; Cui, Y.; He, Y.; Wu, C.; Krishna, R.; Chen, B.; Qian, G. *J. Mater. Chem. A* **2014**, *2*, 2628.
- (28) Duan, J.; Jin, W.; Krishna, R. *Inorg. Chem.* **2015**, *54*, 4279.
- (29) Yoon, J. W.; Lee, J. S.; Lee, S.; Cho, K. H.; Hwang, Y. K.; Daturi, M.; Jun, C.-H.; Krishna, R.; Chang, J.-S. *Chem. - Eur. J.* **2015**, *21*, 18431.
- (30) (a) Krishna, R. *RSC Adv.* **2015**, *5*, 52269. Da Silva, F. A.; Rodrigues, A. E. *AIChE J.* **2001**, *47*, 341. (b) Grande, C. A.; Poplow, F.; Rodrigues, A. E. *Sep. Sci. Technol.* **2010**, *45*, 1252.
- (31) (a) Li, L.; Krishna, R.; Wang, Y.; Yang, J.; Wang, X.; Li, J. *J. Mater. Chem. A* **2016**, *4*, 751. (b) Li, L.; Wang, Y.; Yang, J.; Wang, X.; Li, J. *J. Mater. Chem. A* **2015**, *3*, 22574. (c) Sato, H.; Kosaka, W.; Matsuda, R.; Hori, A.; Hijikata, Y.; Belosludov, R. V.; Sakaki, S.; Takata, M.; Kitagawa, S. *Science* **2014**, *343*, 167.
- (32) (a) Kanoh, H.; Kondo, A.; Noguchi, H.; Kajiro, H.; Tohdoh, A.; Hattori, Y.; Xu, W.-C.; Moue, M.; Sugiura, T.; Morita, K.; Tanaka, H.; Ohba, T.; Kaneko, K. *J. Colloid Interface Sci.* **2009**, *334*, 1. (b) Aguado, S.; Bergeret, G.; Titus, M. P.; Moizan, V.; Nieto-Draghi, C.; Bats, N.; Farrusseng, D. *New J. Chem.* **2011**, *35*, 546.
- (33) Yamazaki, T.; Takahashi, Y.; Yoshida, D. *J. Colloid Interface Sci.* **2011**, *362*, 463.
- (34) Bureekaew, S.; Sato, H.; Matsuda, R.; Kubota, Y.; Hirose, R.; Kim, J.; Kato, K.; Takata, M.; Kitagawa, S. *Angew. Chem., Int. Ed.* **2010**, *49*, 7660.
- (35) Cohen, M. D.; Schmidt, G. M. J.; Sonntag, F. I. *J. Chem. Soc.* **1964**, 2000.
- (36) Yang, S.-Y.; Deng, X.-L.; Jin, R.-F.; Naumov, P.; Panda, M. K.; Huang, R.-B.; Zheng, L.-S.; Teo, B. K. *J. Am. Chem. Soc.* **2014**, *136*, 558.
- (37) Vansant, J.; Toppet, S.; Smets, G.; Declercq, J. P.; Germain, G.; Van Meerssche, M. *J. Org. Chem.* **1980**, *45*, 1565.
- (38) *Materials Studio Modeling Environment*, v6.0.0; Accelrys Software Inc., S. D., 2011.

# *Supporting Information For*

## **An Adsorbate Discriminatory Gate Effect in a Flexible Porous Coordination Polymer for Selective Adsorption of CO<sub>2</sub> over C<sub>2</sub>H<sub>2</sub>**

Maw Lin Foo,<sup>†‡</sup> Ryotaro Matsuda,<sup>†‡</sup> Yuh Hijikata,<sup>‡</sup> Rajamani Krishna,<sup>¶</sup> Hiroshi Sato,<sup>†</sup> Satoshi Horike,<sup>§</sup> Akihiro Hori,<sup>||</sup> Jingui Duan,<sup>†</sup> Yohei Sato,<sup>||#</sup> Yoshiki Kubota,<sup>||#</sup> Masaki Takata,<sup>||#</sup> Susumu Kitagawa<sup>†§||\*</sup>

<sup>†</sup> Institute for Integrated Cell-Material Sciences (WPI-iCeMS), Kyoto University, Yoshida, Sakyo-ku, Kyoto 606-8501, Japan

<sup>¶</sup> Department of Applied Chemistry, Graduate School of Engineering, Nagoya University, Chikusa-ku, Nagoya 464-8603, Japan

<sup>∇</sup> Japan Science and Technology Agency (JST), PRESTO, 4-1-8 Honcho, Kawaguchi, Saitama 332-0012, Japan

<sup>||</sup> RIKEN SPring-8 center, 1-1-1 Kouto, Sayo-cho, Sayo-gun, Hyogo 679-5148, Japan

<sup>‡</sup> Institute of Transformative Bio-Molecules (WPI-ITbM), Nagoya University, Chikusa-ku, Nagoya 464-8602, Japan

<sup>¶</sup> Van 't Hoff Institute for Molecular Sciences, University of Amsterdam, Science Park 904, 1098 XH Amsterdam, The Netherlands

<sup>§</sup> Department of Synthetic Chemistry and Biological Chemistry, Graduate School of Engineering, Kyoto University, Katsura, Nishikyo-ku, Kyoto 615-8510, Japan

<sup>#</sup> Department of Physical Science, Graduate School of Science, Osaka Prefecture University, 1-1 Gakuencho, Naka-ku, Sakai, Osaka 599-8531, Japan

<sup>Φ</sup> Institute of Multidisciplinary Research for Advanced Materials, Tohoku University, 2-1-1 Katahira, Aoba-ku, Sendai 980-8577, Japan

---

<sup>‡</sup>current address: National University of Singapore, Department of Chemistry, 3 Science Drive 3, Singapore 117543.

## Table of Contents:

Experimental Details .....	S3
Table S1: Comparison of CO <sub>2</sub> and C <sub>2</sub> H <sub>2</sub> .....	S5
Table S2: Comparison of CO <sub>2</sub> and C <sub>2</sub> H <sub>2</sub> uptakes and CO <sub>2</sub> /C <sub>2</sub> H <sub>2</sub> selectivity .....	S5
Table S3: Table of parameters obtained by fitting the CO <sub>2</sub> and C <sub>2</sub> H <sub>2</sub> isotherm of <b>1'</b> at 273 K using a dual site Langmuir-Freundlich isotherm .....	S6
Table S4: Theoretical simulations of the most stable state of CO <sub>2</sub> and C <sub>2</sub> H <sub>2</sub> placed between a pair of phenyl rings. ....	S7
Figure S1: Thermal gravimetric analysis of <b>1</b> ⊃DMF and <b>1'</b> .....	S8
Figure S2: Infra-red Spectroscopy of <b>1</b> ⊃DMF and <b>1'</b> .....	S8
Figure S3a: Powder XRD pattern of [Mn(bdc)(dpe)]⊃DMF or <b>1</b> ⊃DMF as synthesized and simulated pattern from single crystal data .....	S9
Figure S3b: Powder XRD pattern of [Mn(bdc)(dpe)] or <b>1'</b> as synthesized and simulated pattern from single crystal data .....	S9
Figure S4: (a) Two-fold interpenetrating structure of <b>1</b> with solvent DMF molecules shown in space-filling representation .....	S10
Figure S5: Sorption isotherms of <b>1'</b> for CO <sub>2</sub> (195 K), CH <sub>4</sub> (195 K), O <sub>2</sub> (195 K), H <sub>2</sub> (77 K) and N <sub>2</sub> (77 K).....	S11
Figure S6: Adsorption isotherm of N <sub>2</sub> at 195 K.....	S12
Figure S7: Plot of the linear region of the CO <sub>2</sub> (cross-section area= 19.5 Å <sup>2</sup> /molecule) isotherm for <b>1'</b> employing the BET equation at 195 K.....	S12
Figure S8a: Adsorption isotherm for <b>1'</b> at 273 and 283 K for CO <sub>2</sub> .....	S13
Figure S8b: Heat of adsorption vs coverage for CO <sub>2</sub> .....	S13
Figure S9a: Adsorption isotherm for <b>1'</b> at 268 and 273 K for C <sub>2</sub> H <sub>2</sub> .....	S14
Figure S9b: Heat of adsorption vs coverage for C <sub>2</sub> H <sub>2</sub> .....	S14
Figure S10: Adsorption isotherms of CO <sub>2</sub> (blue squares) and C <sub>2</sub> H <sub>2</sub> (blue circles) at 273 K for <b>1'</b> fitted to dual-site Langmuir-Freundlich isotherm.....	S15
Figure S11a: Gas chromatograms for gas mixtures of CO <sub>2</sub> and C <sub>2</sub> H <sub>2</sub> . (A) A 1:1 mixture of CO <sub>2</sub> and C <sub>2</sub> H <sub>2</sub> before adsorption. (B) Adsorbed gases on <b>1'</b> in 100 kPa of a mixed gas atmosphere (CO <sub>2</sub> /C <sub>2</sub> H <sub>2</sub> = 1/1) .....	S16
Figure S11b-d: Flow path diagram of gas separation experiment .....	S17, S18
Figure S12: Plot of gate opening pressure (P <sub>go</sub> ) vs inverse of measurement temperature (1/T) for adsorption isotherms of C <sub>2</sub> H <sub>2</sub> measured at 195 (black) 220 (blue), 240 (magenta), 246 (green) K .....	S20
Figure S13a: LeBail fit of <b>1</b> ⊃CO <sub>2</sub> .....	S21
Figure S13b: Preliminary peak indexing attempts for <b>1</b> ⊃ C <sub>2</sub> H <sub>2</sub> .....	S19
Figure S14: Photograph of polycrystalline powders of <b>1'</b> (left) and <b>2</b> (right).....	S22
Figure S15a: (top) <sup>1</sup> H NMR of as-synthesized <b>1</b> ⊃DMF with assignment of protons (bottom) <sup>1</sup> H NMR of <b>1</b> ⊃DMF after irradiation for 1 week, showing mostly <b>1</b> with the presence of a small proportion of <b>2</b> .....	S23
Figure S15b: (top) <sup>1</sup> H NMR of <b>1'</b> as synthesized with assignment of protons (bottom) <sup>1</sup> H NMR of <b>1'</b> after irradiation for a week, showing the conversion to <b>2</b> .....	S23
Figure S16: Mass-spectrometry of digested <b>2</b> with good agreement between actual and simulated data of the molecular ion peak of tpcb .....	S25
Figure S17: TGA of <b>1'</b> and <b>2</b> under flowing N <sub>2</sub> .....	S26
Figure S18a: Powder X-ray diffraction (λ= 1.54 Å) of <b>1'</b> and <b>2</b> .....	S27
Figure S18b: Synchrotron Powder X-ray diffraction (λ= 0.80 Å) of <b>1'</b> and <b>2</b> .....	S27
Figure S19: The result of a Rietveld refinement of <b>2</b> using the proprietary software rwp946.....	S28
Figure S20: Sorption isotherms of <b>2</b> under O <sub>2</sub> at 90 K.....	S29
ORTEP model for <b>1</b> .....	S30
ORTEP model for <b>1'</b> .....	S31
Asymmetric unit of <b>2</b> .....	S32
Table S5: Rietveld refinement parameters for <b>2</b> .....	S33
References .....	S34

## Experimental Details

*IAST modelling* Selectivity Prediction for Binary Mixture Adsorption: Ideal adsorbed solution theory (IAST) was used to predict binary mixture adsorption from the experimental pure-gas isotherms.<sup>S1</sup> In order to perform the integrations required by IAST, the single-component isotherms should be fitted by a proper model. There is no restriction on the choice of the model to fit the adsorption isotherm, but data over the pressure range under study should be fitted very precisely.<sup>S2</sup> The dual-site Langmuir–Freundlich equation was used to fit the experimental isotherms of pure CO<sub>2</sub> and pure C<sub>2</sub>H<sub>2</sub> at 273 K. Table S3 and Figure S10 shows that the dual-site Langmuir–Freundlich equation fits the single-component isotherms of CO<sub>2</sub> and C<sub>2</sub>H<sub>2</sub> extremely well with R<sup>2</sup> value of 0.99979 and 0.99999 respectively. Hence, the fitted isotherm parameters were applied to perform the necessary integrations in IAST.

$$q = q_{m1} * \frac{b_1 P^{1/n_1}}{1 + b_1 P^{1/n_1}} + q_{m2} * \frac{b_2 P^{1/n_2}}{1 + b_2 P^{1/n_2}}$$

P is the pressure of the bulk gas at equilibrium with the adsorbed phase (kPa); q is the adsorbed amount per mass of adsorbent (mol/kg), q<sub>m1</sub> and q<sub>m2</sub> are the saturation capacities of sites 1 and 2 (mol/kg);

b<sub>1</sub> and b<sub>2</sub> are the affinity coefficients of sites 1 and 2 (1/kPa), n<sub>1</sub> and n<sub>2</sub> represent the deviations from an ideal homogeneous surface.

### *Breakthrough simulations*

Transient breakthrough simulations were performed using the simulation methodology described by Krishna<sup>S3</sup> For the breakthrough simulations, the following parameter values were used: length of packed bed, L = 0.3 m; voidage of packed bed, ε = 0.4; superficial gas velocity at inlet, u = 0.04 m/s. The framework density of 1' used is 1342 kg/m<sup>3</sup>. The breakthrough simulations were performed for a total gas pressure of 200 kPa, and constant temperature of 273 K. The transient breakthrough simulation results are presented in terms of a dimensionless time, τ, defined by dividing the actual time, t, by the characteristic time, Lε/u.

### *Heat of adsorption by Virial Equation:*

For adsorption isotherms of CO<sub>2</sub> (273 and 283 K) and C<sub>2</sub>H<sub>2</sub> (268 and 273 K), fits were performed using the virial equation with R software.

$$\ln(p) \sim \ln(n) + (1/T) * (a_0 + a_1 * n + a_2 * n^2) + (b_0 + b_1 * n)$$

where p = pressure/ Pa, n = amount of adsorption / mmol·mol<sup>-1</sup>, T = temperature / K

a<sub>0</sub>, a<sub>1</sub>, a<sub>2</sub>, a<sub>3</sub>, b<sub>0</sub>, b<sub>1</sub> = fitting parameters.

The heat of adsorption, Q<sub>st</sub> in kJ·mol<sup>-1</sup> is given by:

$$Q_{st} = -R \sum_{i=0}^2 a_i n^i$$

Here, Q<sub>st</sub> is the coverage-dependent isosteric heat of adsorption and R is the universal gas constant

*Gas separation experiment under dynamic conditions (Please also see Figure S11b-f):*

The steps below were carried out similar to steps carried out previously.<sup>S4</sup>

1. Pre-treatment:

The powder sample of [Mn(bdc)(dpe)] or **1'** was set on a cryostat system and heated to 393 K under vacuum condition (below  $10^{-2}$  Pa) for 10 h.

2. Adsorption process:

The temperature was decreased from 393 to 273 K under vacuum. Then once the temperature reached to 273 K, a mixture gas of CO<sub>2</sub> and C<sub>2</sub>H<sub>2</sub> (CO<sub>2</sub> = 50%, controlled by mass flow controllers, flow rate at 7.8 ml/min) was flowing at ambient pressure, and the temperature was kept at 273 K for 1 h under flowing mixture gas.

3. Evacuation of the non-adsorbed gas:

The temperature was decreased from 273 to 200 K under flowing mixture. The remained gas in the chamber and gas lines connected to the cryostat was quickly evacuated to 400 Pa at 200 K not to release the adsorbed gas.

4. Release and detection of the adsorbed gas:

After the evacuation, the sample chamber was closed and the temperature increased to 353 K for releasing the adsorbed gas. The released gas was examined with gas chromatography and the ratio between CO<sub>2</sub> and C<sub>2</sub>H<sub>2</sub> was evaluated from the chromatogram. Gas chromatography equipment (GC-2014; SHIMADZU) with a packed column was used to analyze the released gas. The column temperature was kept at 80 °C during the measurements.

The partition coefficient  $\alpha$  is defined as

$$\alpha = (X_{CO_2}/Y_{CO_2})/(X_{C_2H_2}/Y_{C_2H_2}) = (X_{CO_2}/X_{C_2H_2})/(Y_{CO_2}/Y_{C_2H_2})$$

where:

X<sub>CO<sub>2</sub></sub> = the concentration of CO<sub>2</sub> in the adsorbed phase

Y<sub>CO<sub>2</sub></sub> = the concentration of CO<sub>2</sub> in the feed gas

X<sub>C<sub>2</sub>H<sub>2</sub></sub> = the concentration of C<sub>2</sub>H<sub>2</sub> in the adsorbed phase

Y<sub>C<sub>2</sub>H<sub>2</sub></sub> = the concentration of C<sub>2</sub>H<sub>2</sub> in the feed gas

Table S1: Comparison of CO<sub>2</sub> and C<sub>2</sub>H<sub>2</sub>.

	Size/Å	b.p./K	Dipole	Quadrupole x10 <sup>-40</sup> / Cm <sup>2</sup>
<b>CO<sub>2</sub></b>	3.3	195	0	-13.4
<b>C<sub>2</sub>H<sub>2</sub></b>	3.3	189	0	+20.5







Table S2: Comparison of CO<sub>2</sub> and C<sub>2</sub>H<sub>2</sub> uptake and its CO<sub>2</sub>/C<sub>2</sub>H<sub>2</sub> selectivity in porous coordination compounds and their hybrids (adapted from ref S12).

Coordination polymer	CO <sub>2</sub> (ml/g STP)	C <sub>2</sub> H <sub>2</sub> (ml/g STP)	V <sub>CO2</sub> /V <sub>C2H2</sub>	Condition	Reference
Cu <sub>2</sub> (pzdc) <sub>2</sub> (pyz)	4	42	0.1	270 K 4.5 kPa	S5
Cu(etz)	19	70	0.3	298 K 100 kPa	S6
Cu <sub>3</sub> (BTC) <sub>2</sub>	113	201	0.6	295-298 K 100 kPa	S7
Mg(HCOO) <sub>2</sub>	45	66	0.7	298 K 100 kPa	S8
Mn(HCOO) <sub>2</sub>	38	51	0.7	298 K 100 kPa	S8
Cu(PF <sub>6</sub> ) <sub>2</sub> (bpetha) <sub>2</sub>	135	78	1.7	195 K 100 kPa	S9
[Co(HL <sub>dc</sub> )	240	140	1.7	195 K 100 kPa	S10
Zn <sub>2</sub> (bdc) <sub>2</sub> (DABCO)⊃DSB	140	73	1.9	195 K 97 kPa	S11
K <sub>2</sub> [Cr <sub>3</sub> O(OOCH) <sub>6</sub> (4-ethylpyridine) <sub>3</sub> ] <sub>2</sub> [a-SiW <sub>12</sub> O <sub>40</sub> ]	11.5	2.4	4.8	278 K 100 kPa	S12
Cu <sub>2</sub> (MFDI) (ZJU-60)	178.7	97.7	1.8	273 K 100 kPa	S13
<b>[Mn(bdc)(dpe)]</b>	<b>46.8</b>	<b>7.3</b>	<b>6.4</b>	<b>273 91 kPa</b>	<b>This work</b>

Table S3: Table of parameters obtained by fitting the CO<sub>2</sub> and C<sub>2</sub>H<sub>2</sub> isotherms of **1'** at 273 K using a dual-site Langmuir-Freundlich isotherm.

	CO <sub>2</sub>	C <sub>2</sub> H <sub>2</sub>
<b>R<sup>2</sup></b>	0.99979	0.99999
<b>q<sub>m1</sub></b>	0.3839	3.0986
<b>q<sub>m2</sub></b>	9.7316	0.001141
<b>b<sub>1</sub></b>	0.01521	0.01477
<b>b<sub>2</sub></b>	5.7071E-6	15.6487
<b>n<sub>1</sub></b>	0.8531	1.0940
<b>n<sub>2</sub></b>	1.7742	1.1173E-11

Table S4: Theoretical simulations of the most stable state of CO<sub>2</sub> and C<sub>2</sub>H<sub>2</sub> placed between a pair of phenyl rings. The original distance between the benzene rings are 6.924 Å.

	CO <sub>2</sub>	C <sub>2</sub> H <sub>2</sub>
		
		
		
benzene-benzene spacing (Å)	6.575	8.324
MP2 (kcal/mol)	-4.6	-5.8
HF (kcal/mol)	+1.9	-0.6
DFT-D3 (kcal/mol)	-3.0	-4.0



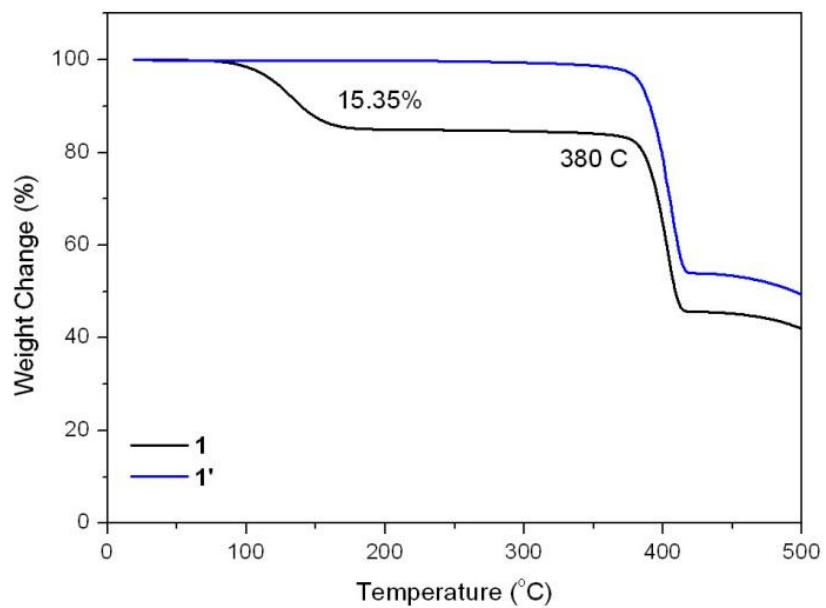


Figure S1: Thermal gravimetric analysis of **1**DMF and **1'**. Theoretical weight loss of one DMF for **1**DMF: 15.35%

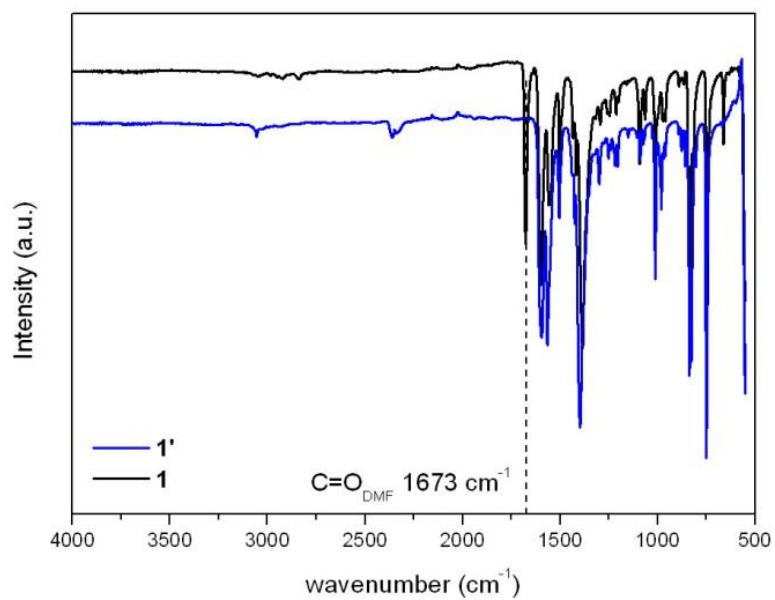


Figure S2: Infra-red spectroscopy of **1**DMF and **1'**.

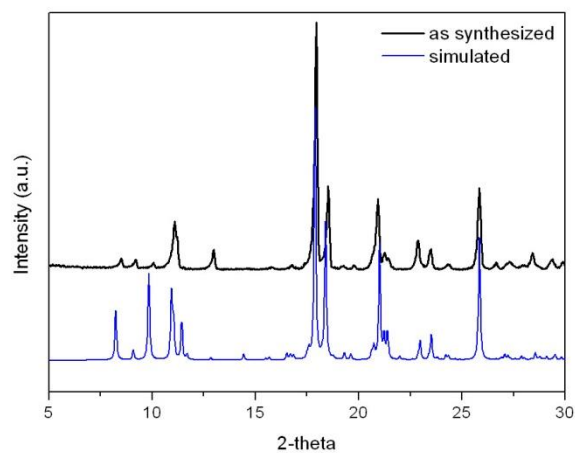


Figure S3a: Powder XRD pattern of  $[\text{Mn}(\text{bdc})(\text{dpe})]\cdot\text{DMF}$  or  $\mathbf{1}\cdot\text{DMF}$  as synthesized and simulated pattern from single crystal data.

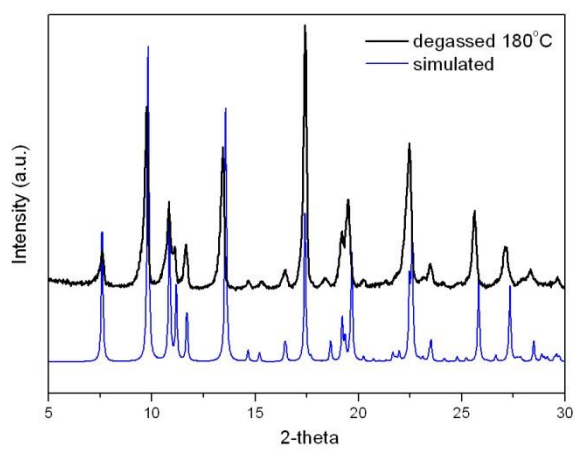


Figure S3b: Powder XRD pattern of  $[\text{Mn}(\text{bdc})(\text{dpe})]$  or  $\mathbf{1}'$  as synthesized and simulated pattern from single crystal data.

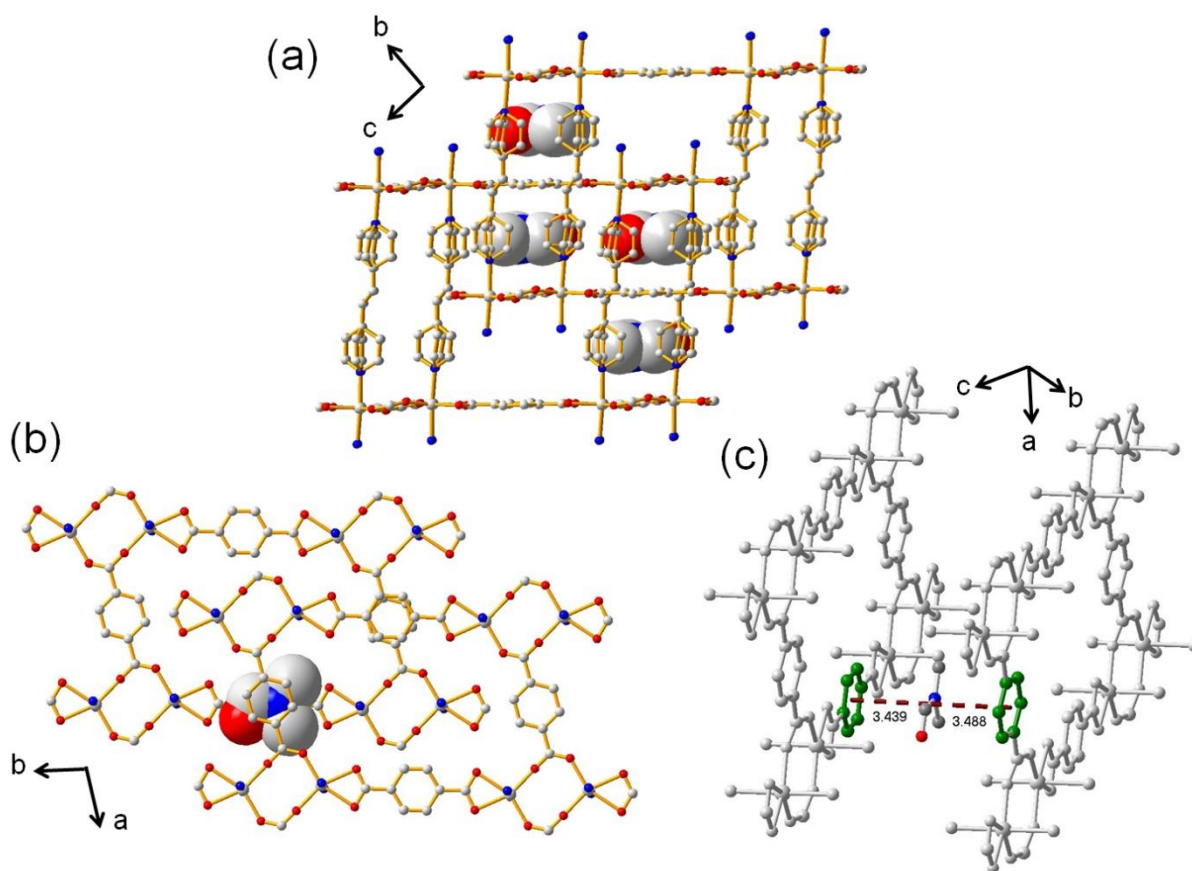


Figure S4: (a) Two-fold interpenetrating structure of **1** with solvent DMF molecules shown in space-filling representation. Blue spheres represent nitrogen, red spheres oxygen, gray spheres carbon (b) Alternate view of two-fold interpenetrating structure of **1** with one solvent DMF molecule shown (c) Representation of **1** with DMF solvent molecule sandwiched by two phenyl rings (green) from *bdc*.

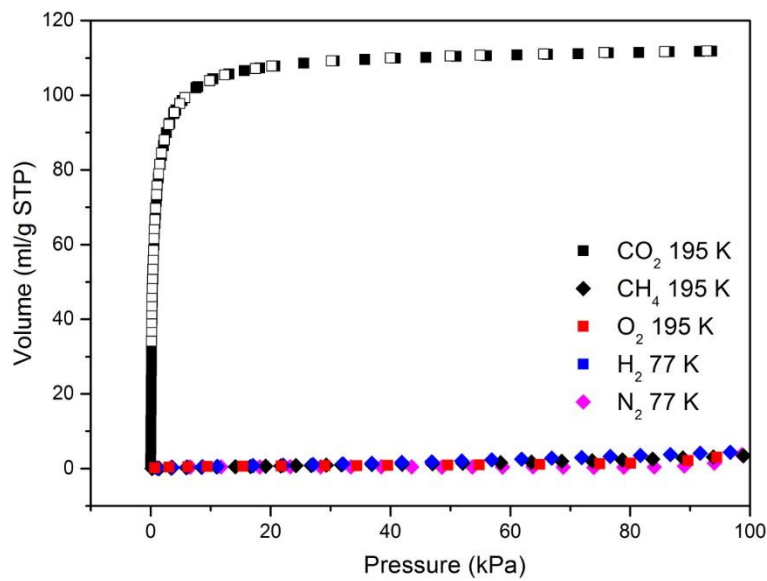


Figure S5: Adsorption isotherms of **1'** for CO<sub>2</sub> (195 K), CH<sub>4</sub> (195 K), O<sub>2</sub> (195 K), H<sub>2</sub> (77 K) and N<sub>2</sub> (77 K). For simplicity, desorption isotherm is shown only for CO<sub>2</sub>. The lack of adsorption for H<sub>2</sub> is probably due to its low boiling point (20 K) and weak interaction with the pore surface despite the molecular size of H<sub>2</sub> being small enough (kinetic diameter: 2.89 Å).

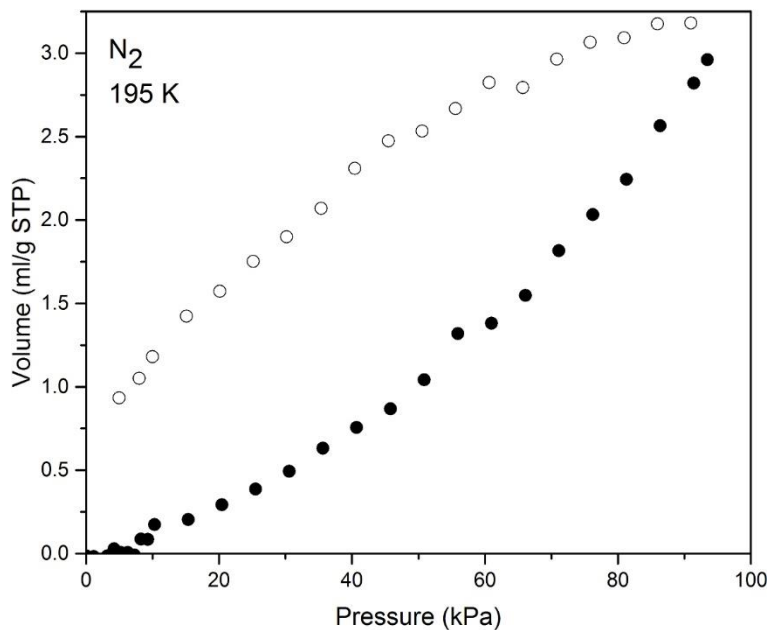


Figure S6: Adsorption isotherm of N<sub>2</sub> at 195 K.

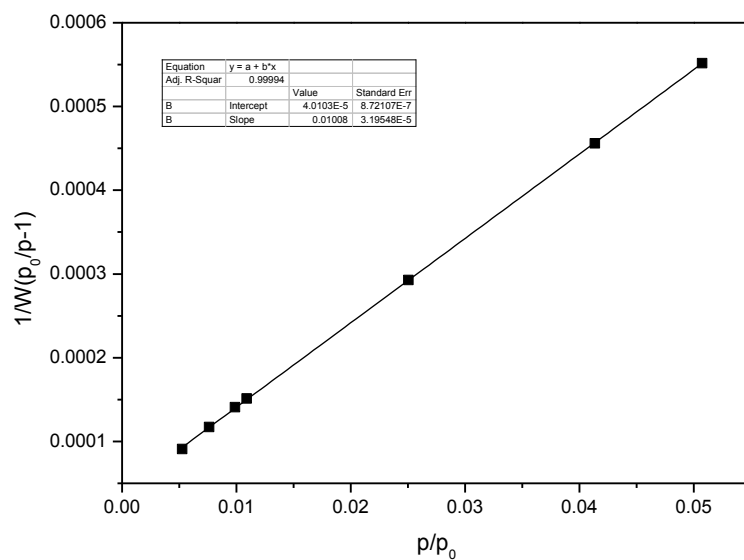


Figure S7: Plot of the linear region of the CO<sub>2</sub> (cross-section area= 19.5 Å<sup>2</sup>/molecule) isotherm for 1' employing the BET equation at 195 K.

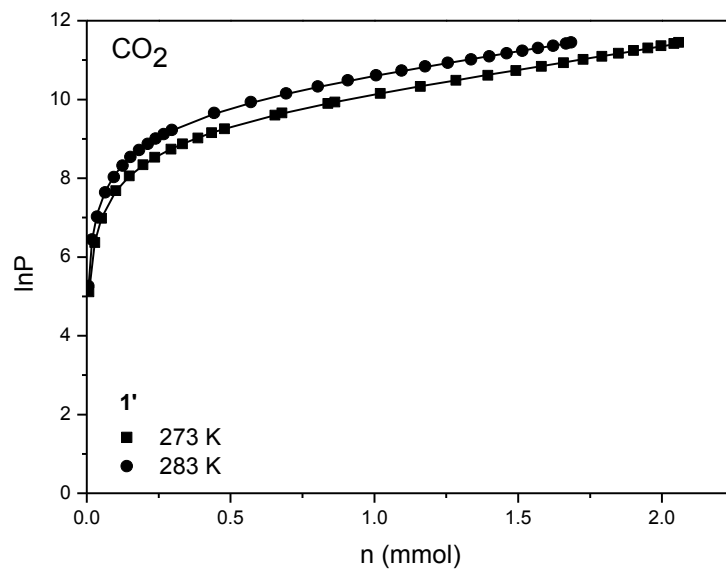


Figure S8a: Adsorption isotherm for  $1'$  at 273 and 283 K for  $\text{CO}_2$ . Solid lines denote fit using virial equation. Obtained parameters:  $a_0 = -3543$ ,  $a_1 = -135$ ,  $a_2 = 49.9$   $b_0 = 22.9$ ,  $b_1 = 0.4799$ .  $R^2 = 0.9999$ .

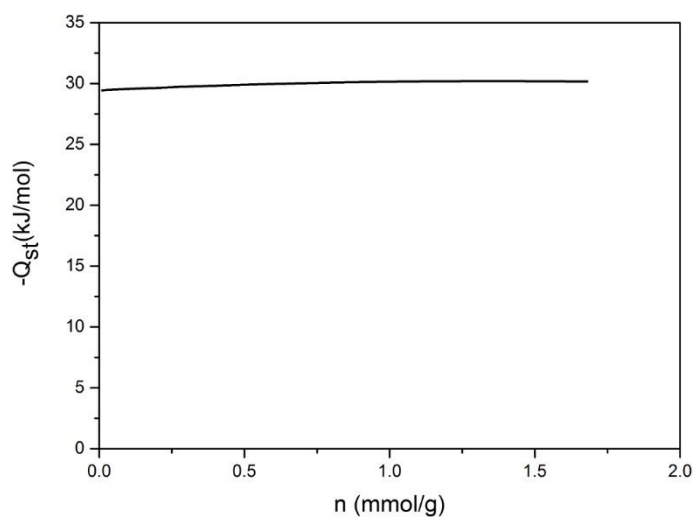


Figure S8b: Heat of adsorption vs coverage for  $\text{CO}_2$ .

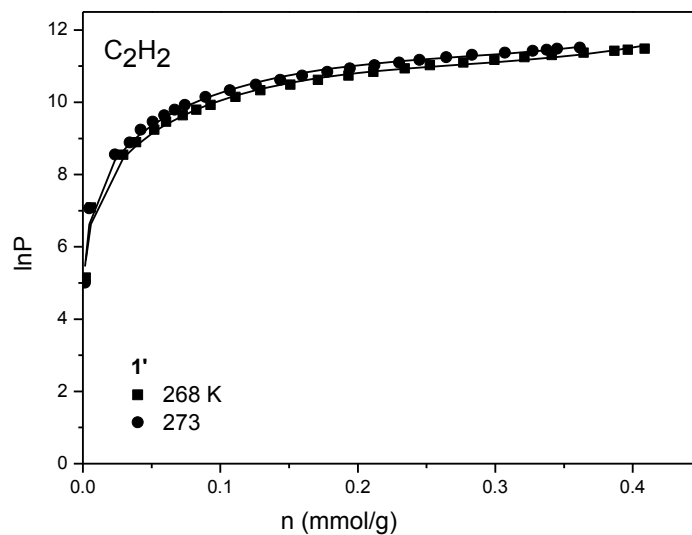


Figure S9a: Adsorption isotherm for **1'** at 268 and 273 K for  $C_2H_2$ . Solid lines denote fit using virial equation. Obtained parameters:  $a_0 = -3328$ ,  $a_1 = 2841$ ,  $a_2 = -13036$ ,  $a_3 = 17863$ ,  $b_0 = 24.1$ .  $R^2 = 0.9919$ .

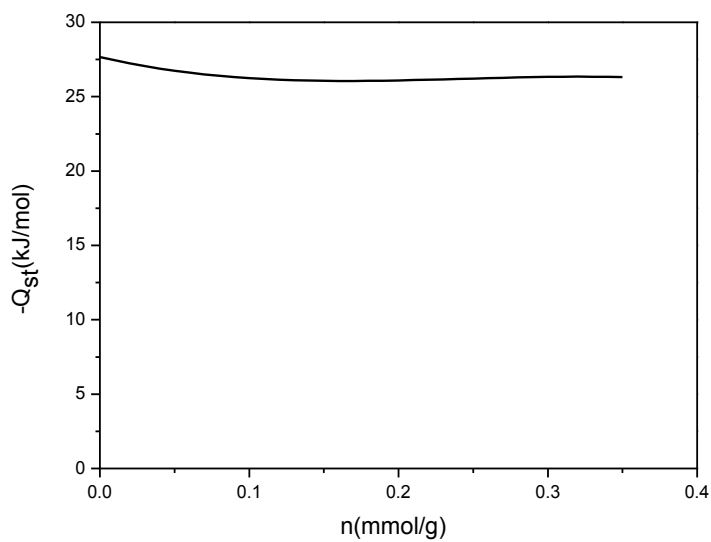


Figure S9b: Heat of adsorption vs coverage for  $C_2H_2$ .

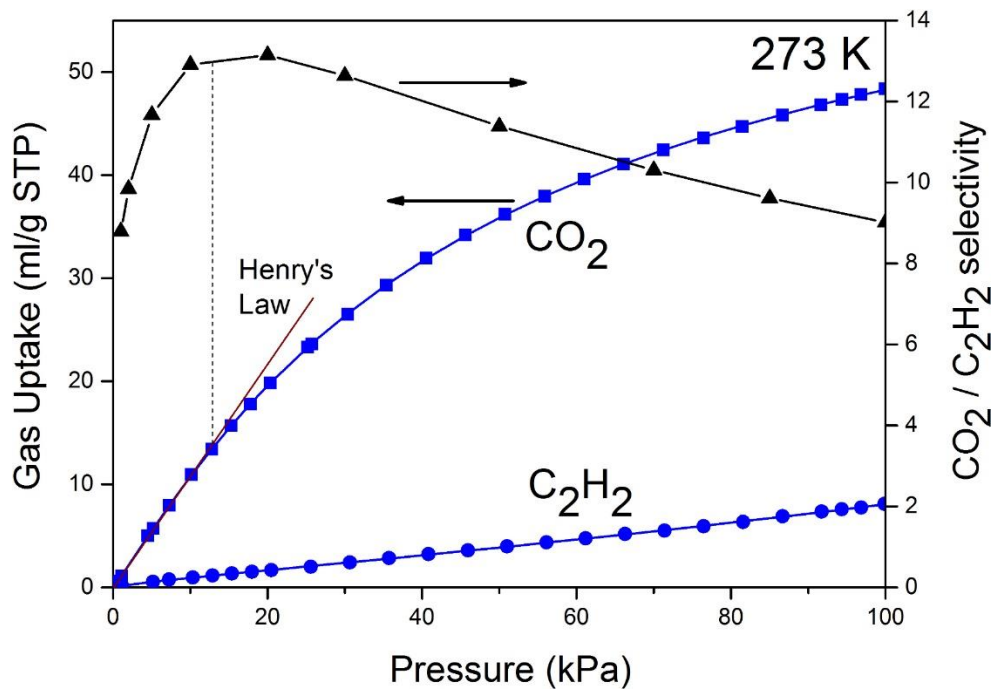


Figure S10: Adsorption isotherms of CO<sub>2</sub> (blue squares) and C<sub>2</sub>H<sub>2</sub> (blue circles) at 273 K for **1'** fitted to dual-site Langmuir–Freundlich isotherm. The CO<sub>2</sub>/C<sub>2</sub>H<sub>2</sub> selectivity calculated by IAST is represented by black triangles. It is noted that the calculated selectivity is increasing in the pressure range corresponding to Henry's Law, i.e.  $n_{\text{ads}} = K_{\text{H}}P$  where  $K_{\text{H}}P$  is Henry's Law Constant.



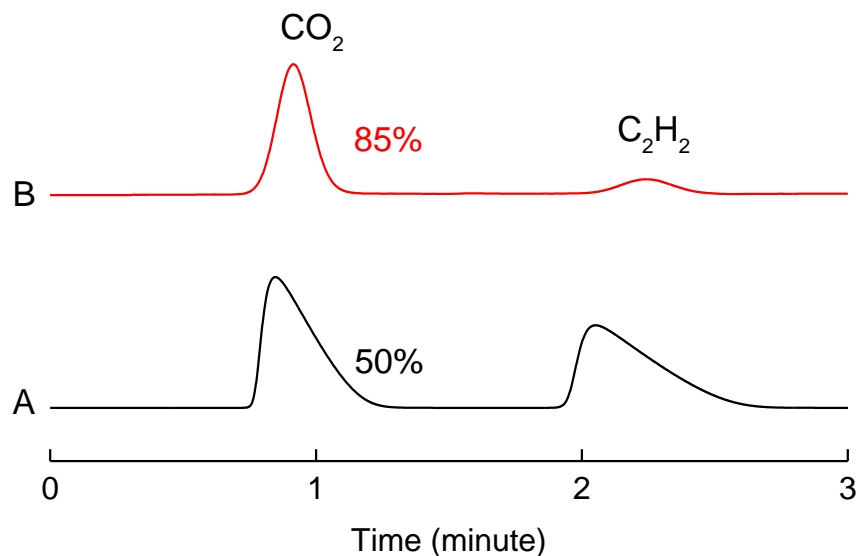


Figure S11a: Gas chromatograms for gas mixtures of  $\text{CO}_2$  and  $\text{C}_2\text{H}_2$ . (A) A 1:1 mixture of  $\text{CO}_2$  and  $\text{C}_2\text{H}_2$  before adsorption. (B) Adsorbed gases on **1'** in 100 kPa of a mixed gas atmosphere ( $\text{CO}_2/\text{C}_2\text{H}_2 = 1/1$ ). Partition coefficient,  $\alpha = (X_{\text{CO}_2}/Y_{\text{CO}_2})/(X_{\text{C}_2\text{H}_2}/Y_{\text{C}_2\text{H}_2}) = 5.7$

Note: *Experimental procedure for gas separation with flow diagrams* (Figure S11b-f)

No. 1. Sample set in the cell

No. 2. Evacuation in vacuum at 393 K for 10 hours (Figure S11b).

No. 3. Gas mixture flowing for 1 hour at 273 K (Figure S11c).

No. 4. Closing the valves of V3 and V4 (Figure S11d).

No. 5. Evacuation of remained gas in the tube (Area 3)

No. 6. Cooling to 200 K quickly.

No. 7. Flush evacuation of remained gas in the tubes and in the sample chamber with quick opening and closing of the valve (V3) (Figure S11e).

No. 8. Closing the valves of V3 and V4 (Figure S11f).

No. 9. Heating to 353 K to disrobe gas from the sample.

No. 10. GC test

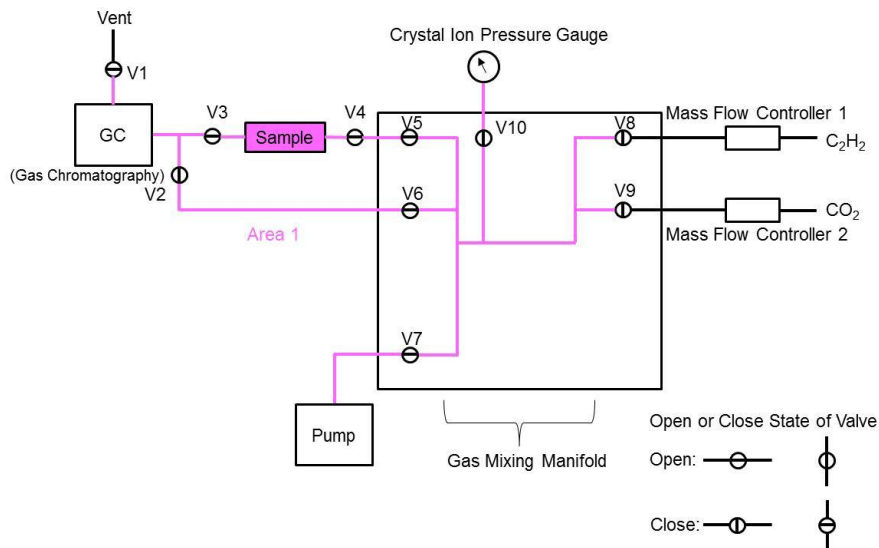


Figure S11b. Flow path diagram of gas separation experiment for the process No. 2.

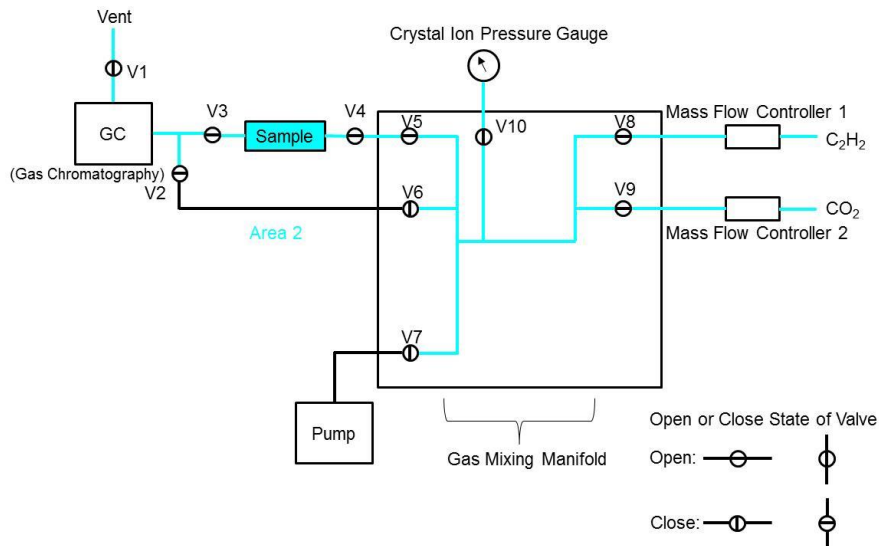


Figure S11c.: Flow path diagram of gas separation experiment for the process No. 3.

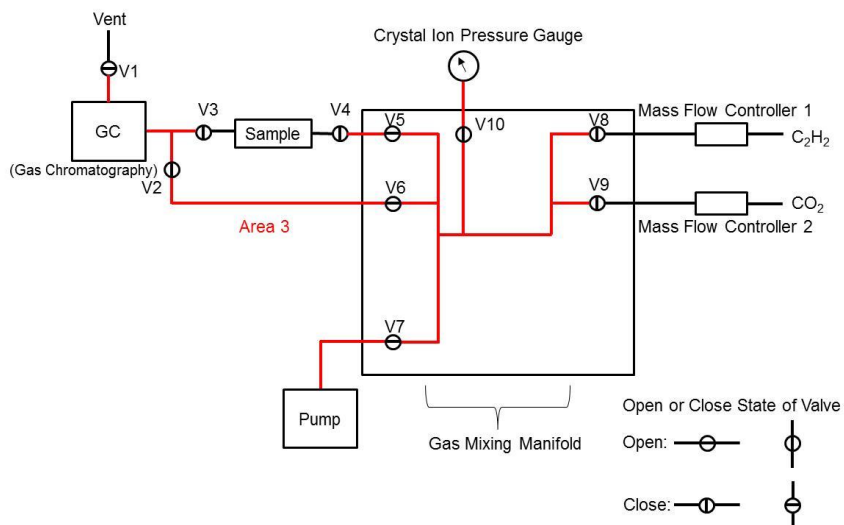


Figure S11d. Flow path diagram of gas separation experiment for the process No. 4, 5 and 6.

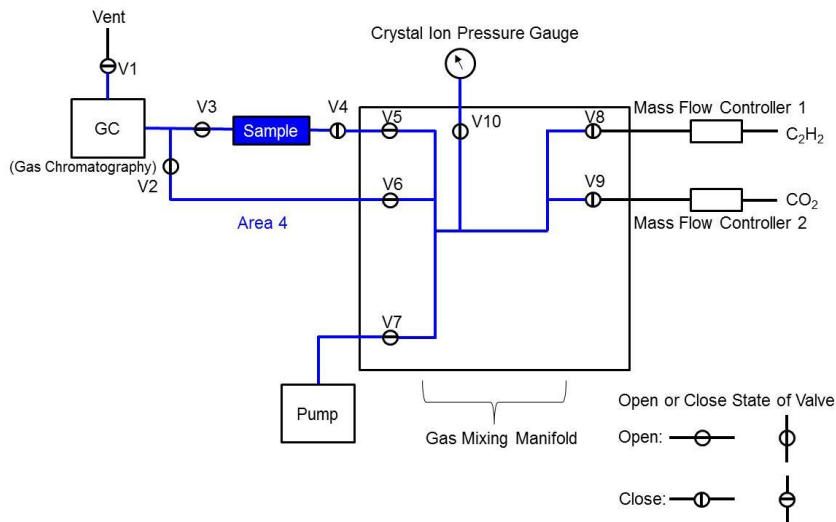


Figure S11e. Flow path diagram of gas separation experiment for the process No. 7.

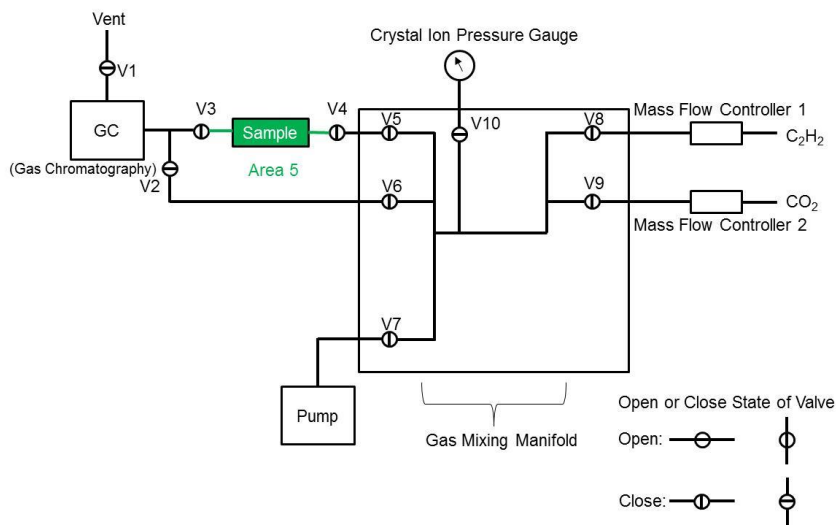


Figure S11f. Flow path diagram of gas separation experiment for the process No. 8 and 9.

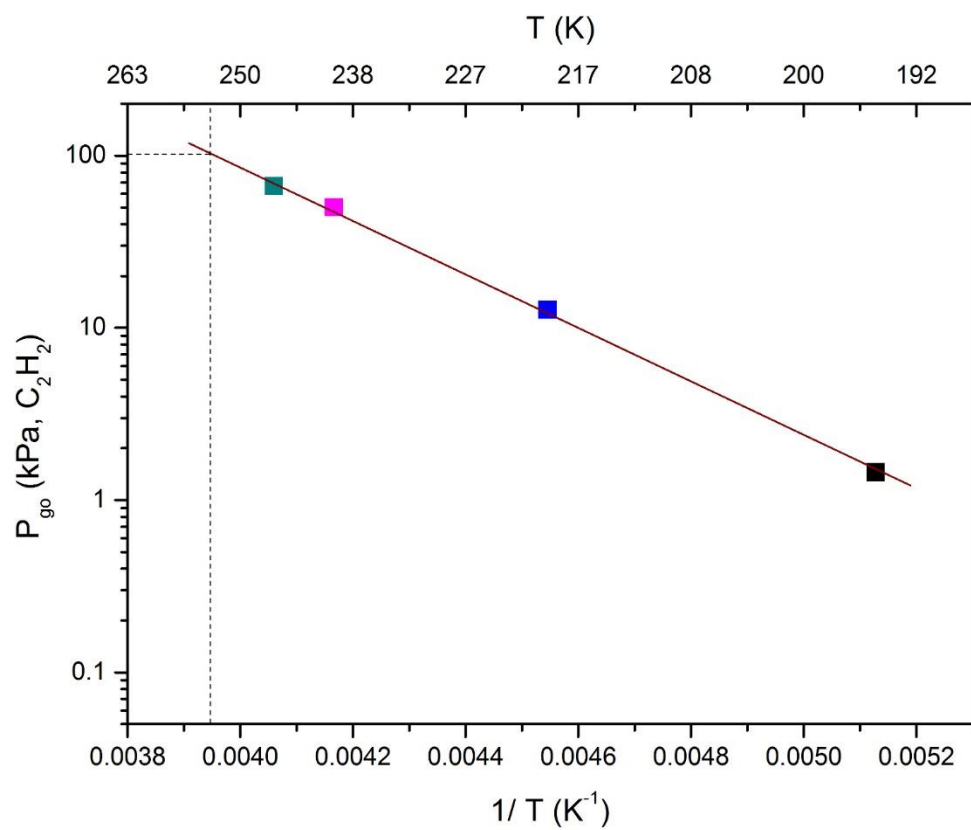


Figure S12: Plot of gate opening pressure ( $P_{go}$ ) vs inverse of measurement temperature ( $1/T$ ) for adsorption isotherms of  $C_2H_2$  measured at 195 (black) 220 (blue), 240 (magenta), 246 (green) K. At  $P_{go} = 100$  kPa (1 atm), the corresponding temperature (252 K) can be obtained (dotted lines).

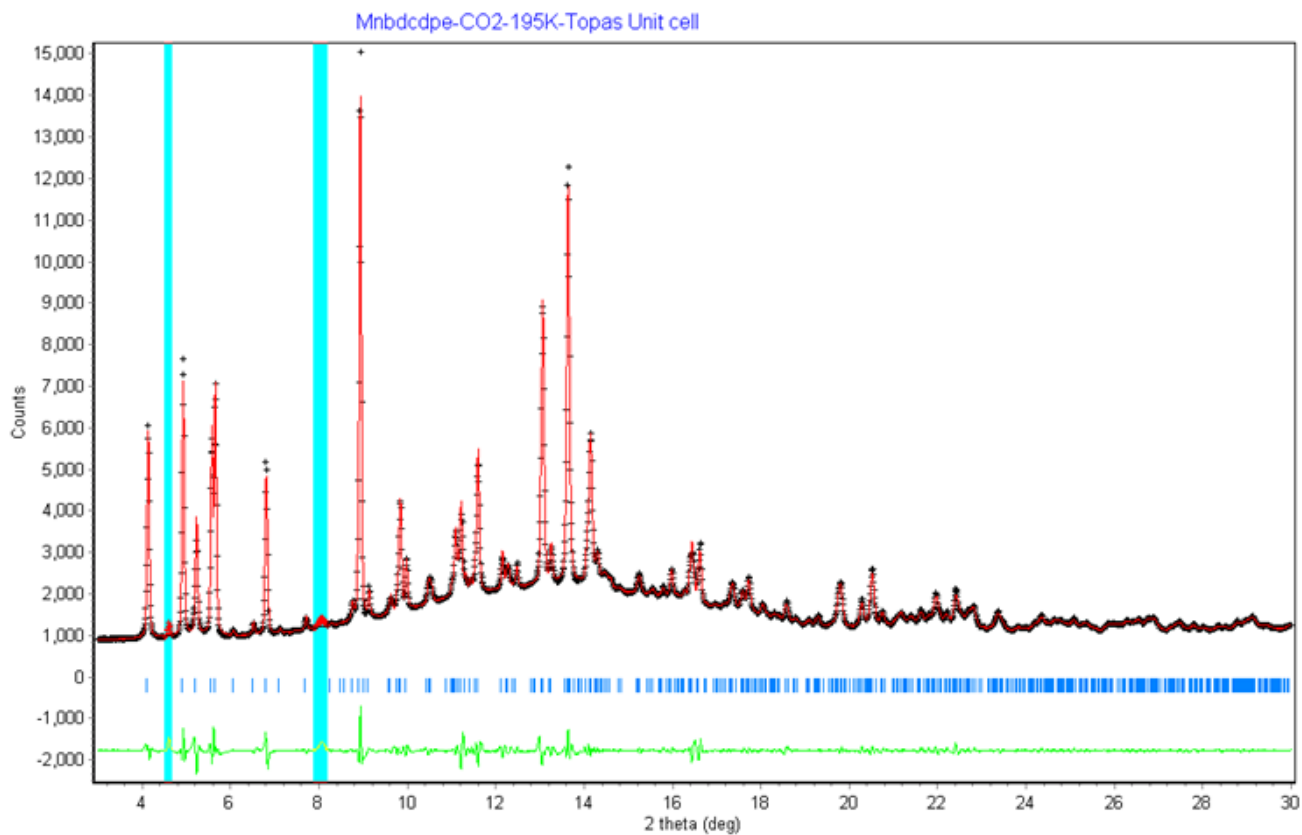


Figure S13a: Le Bail fit of  $\mathbf{1} \supset \text{CO}_2$ .

Note: The result of the refinement is as follows  
 $a = 9.6609(3)$ ,  $b = 11.5232(4)$ ,  $c = 10.5314(2) \text{ \AA}$   
 $\alpha = 105.684(3)$ ,  $\beta = 114.898(2)$ ,  $\gamma = 81.211(2)^\circ$   
 $V = 1022.84 \text{ \AA}^3$   
 $R_p = 1.844$   $R_{wp} = 2.934$   
 $\chi^2 = 1.559$

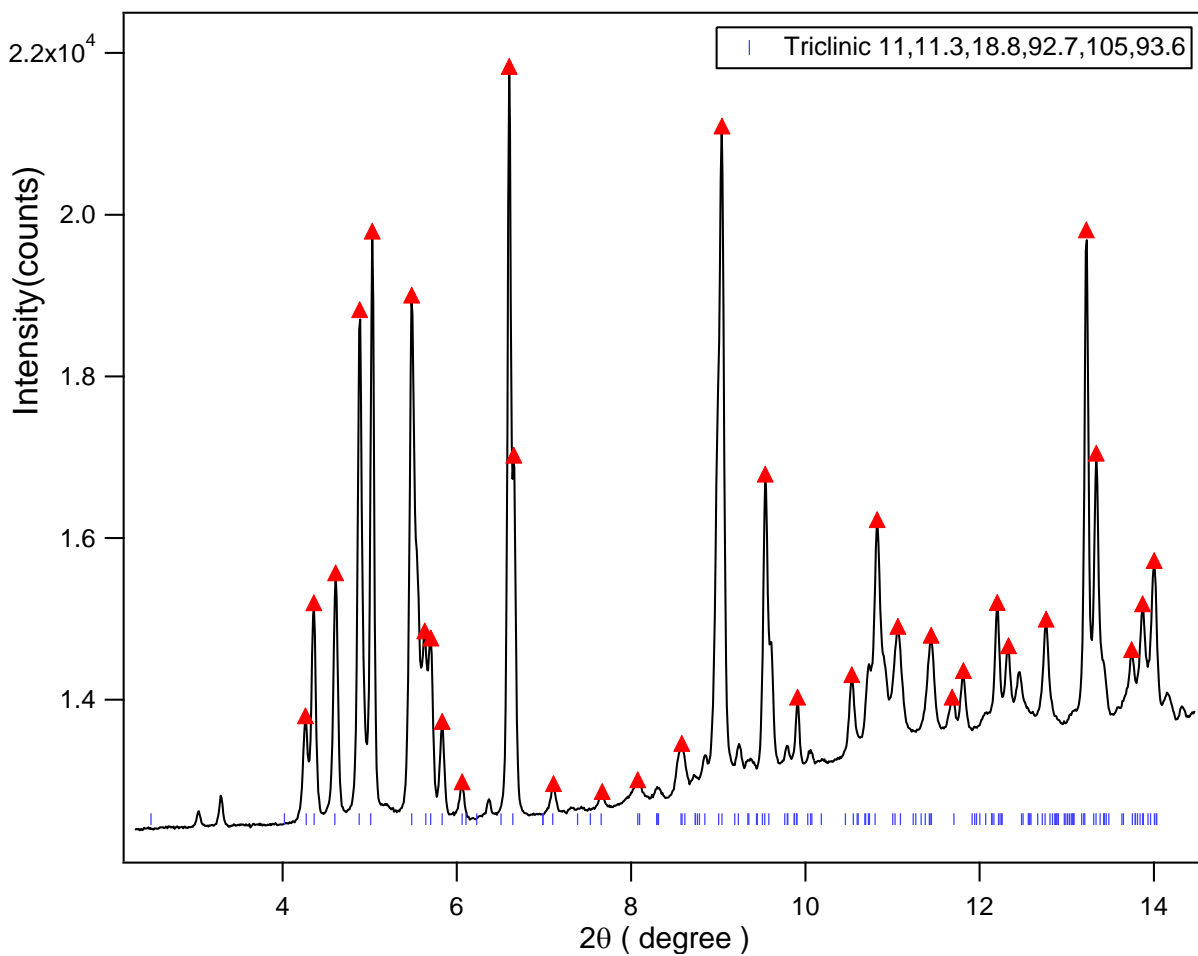


Figure S13b: Preliminary peak indexing attempts for **1**  $\supset$   $\text{C}_2\text{H}_2$ .

Note: The result of the indexing is as follows  
 $a = 11.03862 \text{ \AA}$ ,  $b = 11.34966 \text{ \AA}$ ,  $c = 18.8118 \text{ \AA}$   
 $\alpha = 92.73031^\circ$ ,  $\beta = 104.5771^\circ$ ,  $\gamma = 93.63065^\circ$   
 $V = 2271.45 \text{ \AA}^3$



Figure S14: Photograph of polycrystalline powders of **1'** (left) and **2** (right).

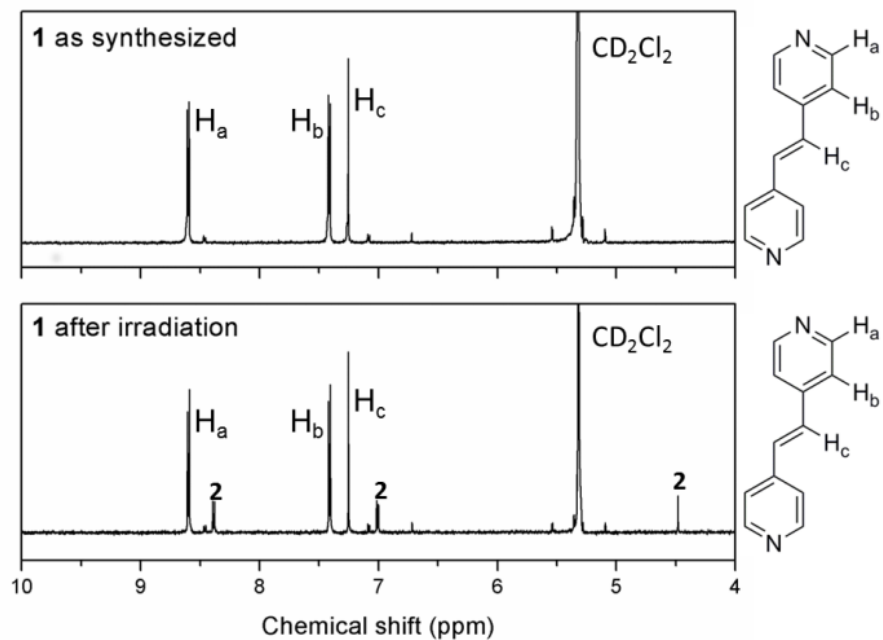


Figure S15a: (top)  $^1\text{H}$  NMR of as-synthesized **1** in  $\text{DMF}$  with assignment of protons (bottom)  $^1\text{H}$  NMR of **1** in  $\text{DMF}$  after irradiation for 1 week, showing mostly **1** with the presence of a small proportion of **2**.

Note:

For as-synthesized **1** in  $\text{DMF}$ ,

$\delta$  8.60 (m, 4H,  $\text{H}_a$ ) 7.61 (m, 4H,  $\text{H}_b$ ) 7.25 (s, 2H,  $\text{H}_c$ ).

For as-synthesized **1** in  $\text{DMF}$  (after irradiation),

$\delta$  8.60 (m, 4H,  $\text{H}_a$ ) 8.38 (m, 0.33H,  $\text{H}_a'$ ) 7.41 (m, 4H,  $\text{H}_b$ ) 7.01 (m, 0.66H,  $\text{H}_b'$ ) 7.25 (s, 2H,  $\text{H}_c$ ) 4.48 (s, 0.33H,  $\text{H}_c'$ ).

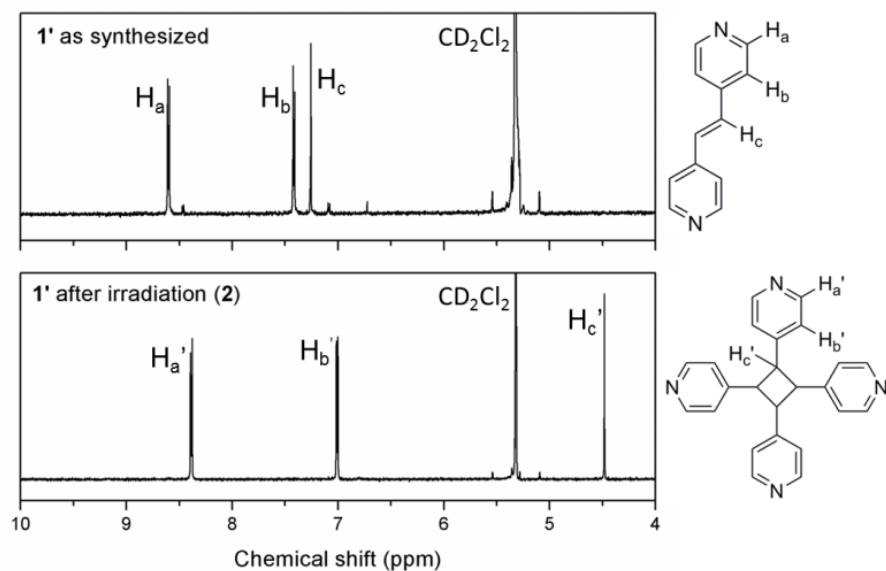


Figure S15b: (top)  $^1\text{H}$  NMR of **1'** as synthesized with assignment of protons (bottom)  $^1\text{H}$  NMR of **1'** after irradiation for a week, showing the conversion to **2**.

For as-synthesized **1'**

$\delta$  8.60 (m, 4H,  $\text{H}_a$ ) 7.41 (m, 4H,  $\text{H}_b$ ) 7.25 (s, 2H,  $\text{H}_c$ ).

For **2**:

$\delta$  8.39 (m, 8H,  $\text{H}_a'$ ) 7.01 (m, 8H,  $\text{H}_b'$ ) 4.48 (s, 4H,  $\text{H}_c'$ ).



Note: Unlike the dried sample **1**, **1**⊃DMF, where the corresponding distance between C=C bonds is 4.712 Å (above the Schmidt's criterion) remained yellow even after photoirradiation. By <sup>1</sup>H NMR (Figure S13a), ~ 8 % of photodimerized product is observed. The small proportion of **2** produced is probably due to gradual loss of solvent from the surface of **1**⊃DMF, leading to the formation of small quantities of **1'** and its subsequent photodimerization. This observation of quantitative dimerization in **1'** is the first report (to the best of our knowledge) of a degassed PCP showing [2+2] photodimerization.

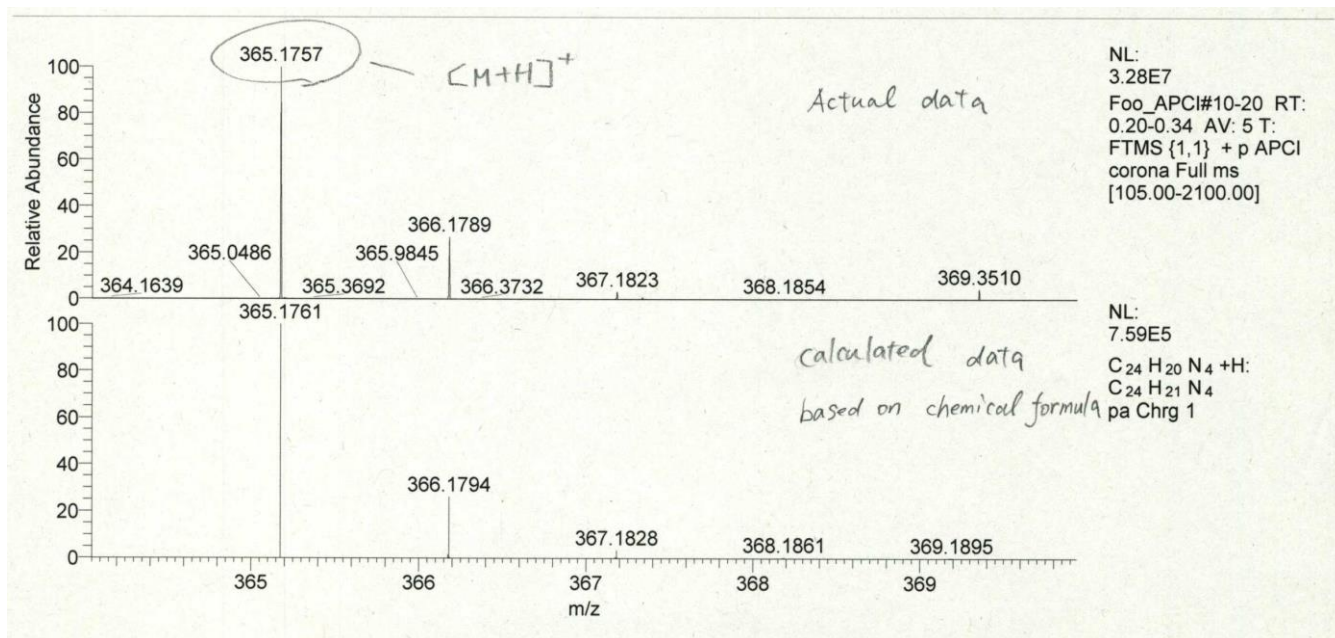


Figure S16: Mass-spectrometry of digested **2** with good agreement between actual and simulated data of the molecular ion peak of tpcb.

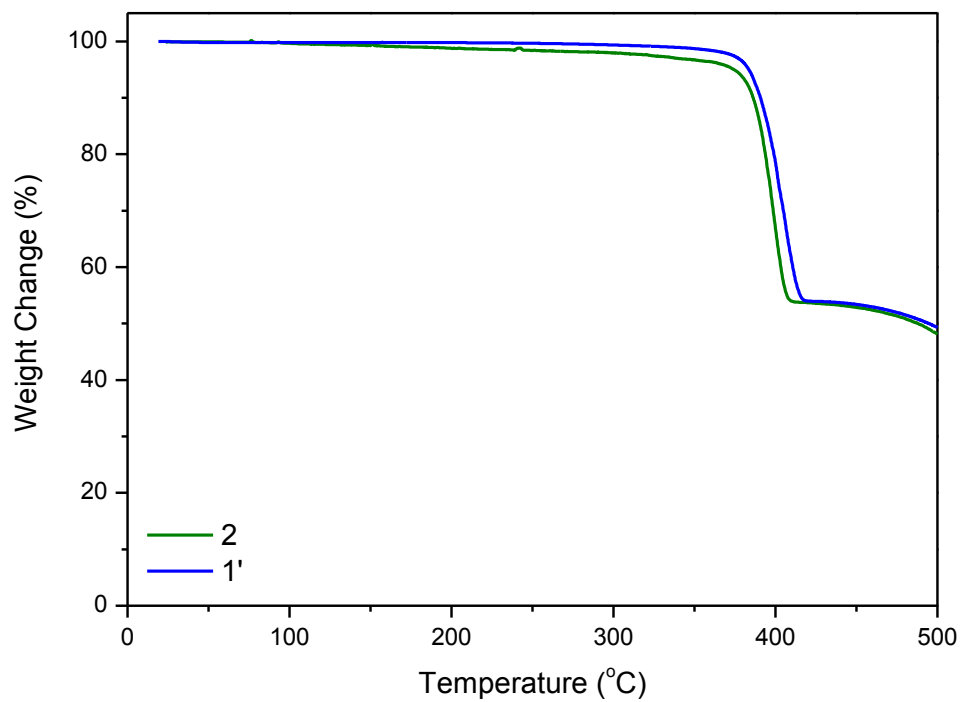


Figure S17: TGA of **1'** and **2** under flowing N<sub>2</sub>.

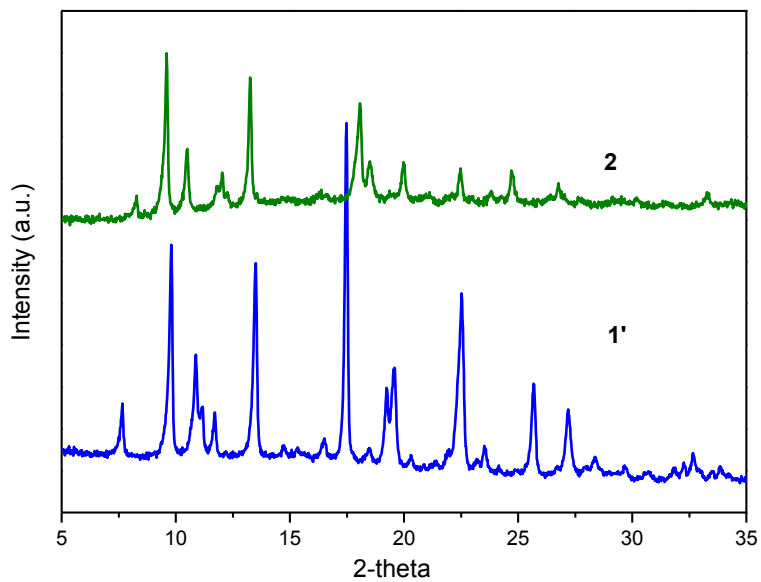


Figure S18a: Powder X-ray diffraction ( $\lambda = 1.54 \text{ \AA}$ ) of **1'** and **2**.

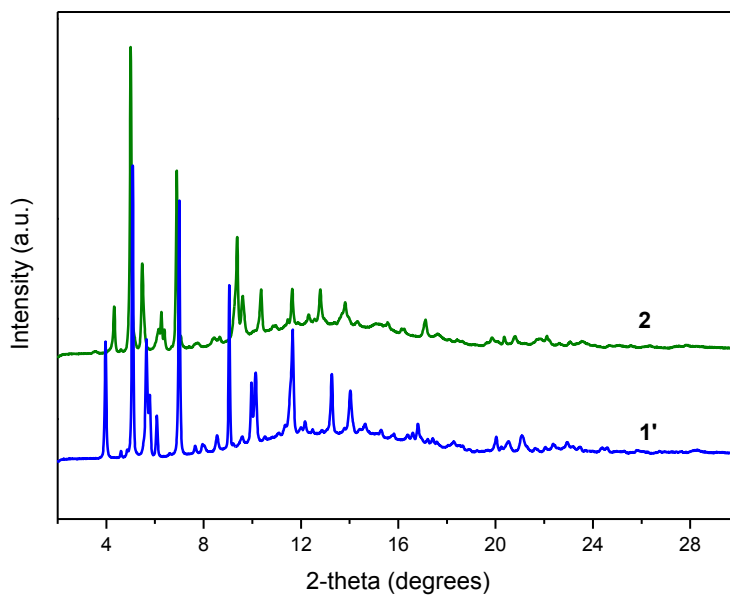


Figure S18b: Synchrotron Powder X-ray diffraction ( $\lambda = 0.80 \text{ \AA}$ ) of **1'** and **2**.

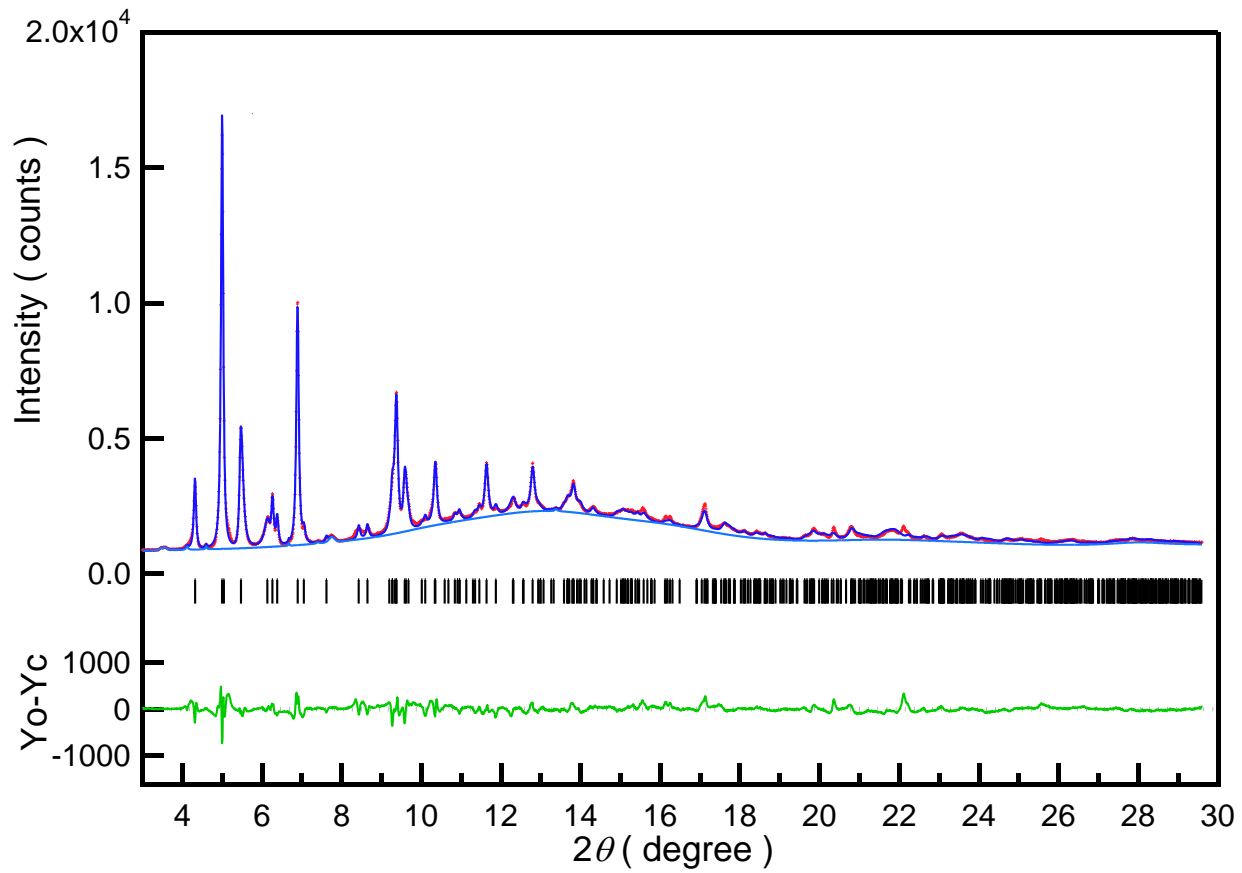


Figure S19: The result of a Rietveld refinement of **2** using the proprietary software rwp946.

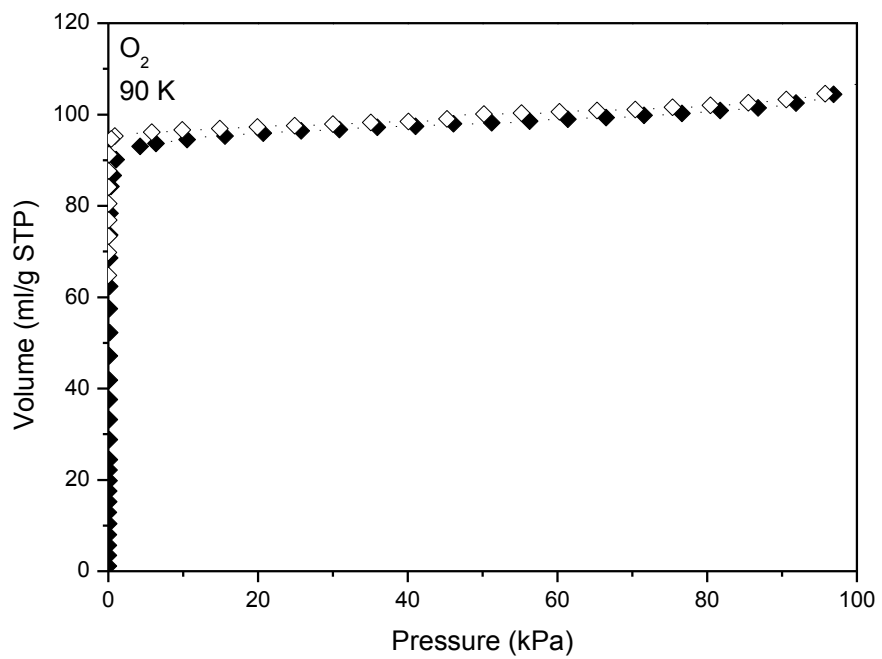
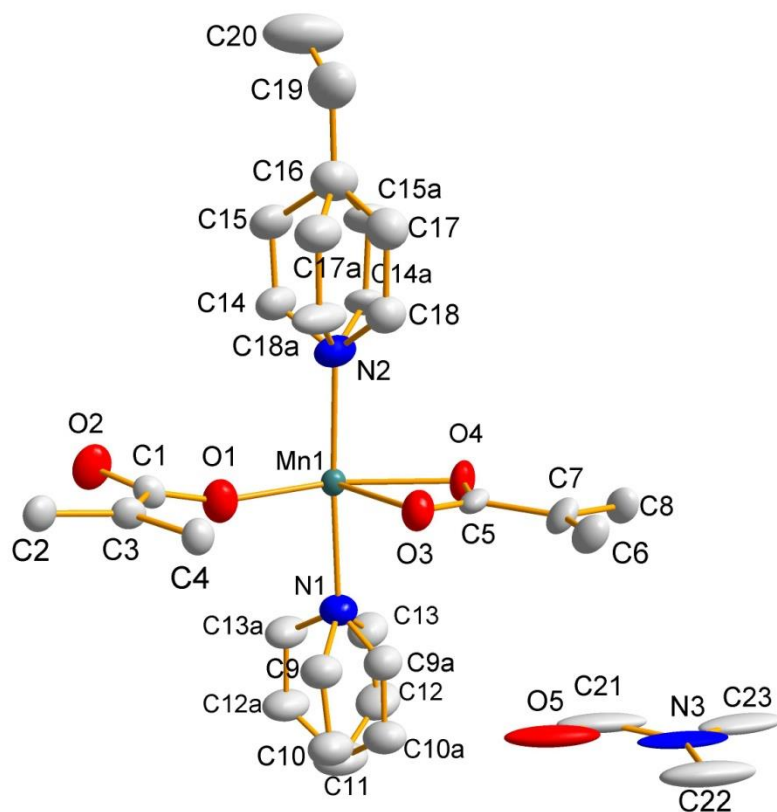


Figure S20: Sorption isotherms of **2** under O<sub>2</sub> at 90 K.

ORTEP model for **1**



Bond distances (Å)

Mn1—O1 2.066(7) Mn1—O4 2.211(6)

Mn1—O2<sup>i</sup> 2.090(4) Mn1—N1 2.270(6)

Mn1—O3 2.305(4) Mn1—N2 2.269(6)

Bond angles (degrees)

O1—Mn1—O2<sup>i</sup> 106.3(2) O3—Mn1—O4 57.4(2)

O1—Mn1—O3 100.2(2) O3—Mn1—N1 87.52(17)

O1—Mn1—O4 157.44(17) O3—Mn1—N2 87.58(18)

O1—Mn1—N1 88.7(2) O4—Mn1—N1 87.8(2)

O1—Mn1—N2 92.3(3) O4—Mn1—N2 89.4(2)

O2<sup>i</sup>—Mn1—O3 153.4(2) N1—Mn1—N2 175.09(19)

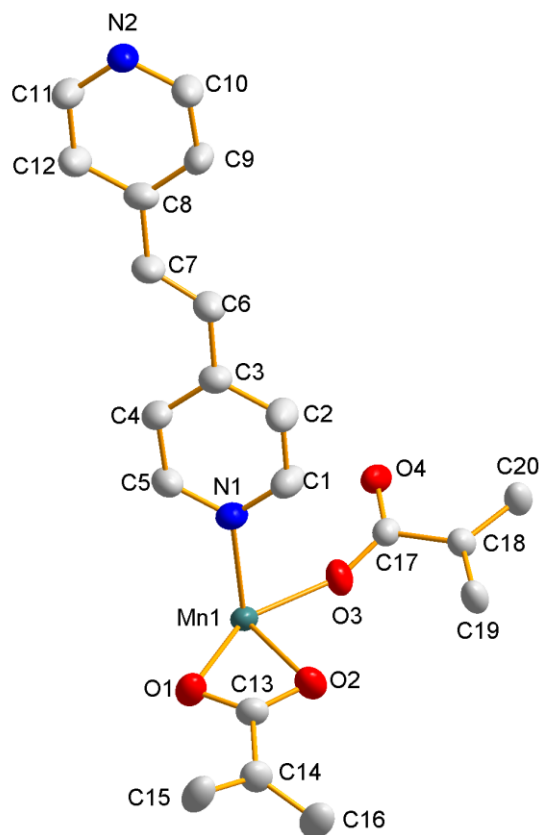
O2<sup>i</sup>—Mn1—O4 96.1(2)

O2<sup>i</sup>—Mn1—N1 90.6(2)

O2<sup>i</sup>—Mn1—N2 93.7(2)

(i) 2-x, -y, -z; (ii) 1-x, -y, -z; (iii) 1-x, 1-y, 1-z; (iv) x, -1+y, 1+z;  
(v) 2-x, -y, 1-z; (vi) 2-x, 1-y, -z; (vii) 1-x, -y, 1-z; (viii) x, y, -1+z;  
(ix) x, y, 1+z; (x) 1-x, 1-y, -z; (xi) x, -1+y, z; (xii) x, 1+y, z;  
(xiii) x, 1+y, -1+z; (xiv) 2-x, 1-y, -1-z; (xv) -1+x, 1+y, z.

ORTEP model for **1'**



Structural parameters for [Mn(bdc)(dpe)], **1'**

Bond distances (Å)

Mn1—O3 2.092(2) Mn1—O1 2.270(2)

Mn1—O4<sup>i</sup> 2.120(2) Mn1—N2<sup>ii</sup> 2.300(3)

Mn1—N1 2.270(3) Mn1—O2 2.305(2)

Bond angles (degrees)

O3—Mn1—O4<sup>i</sup> 120.61(9) O3—Mn1—N2<sup>ii</sup> 87.55(10) N1—Mn1—O2 97.46(9)

O3—Mn1—N1 89.65(10) O4<sup>i</sup>—Mn1—N2<sup>ii</sup> 87.14(9) O1—Mn1—O2 57.88(8)

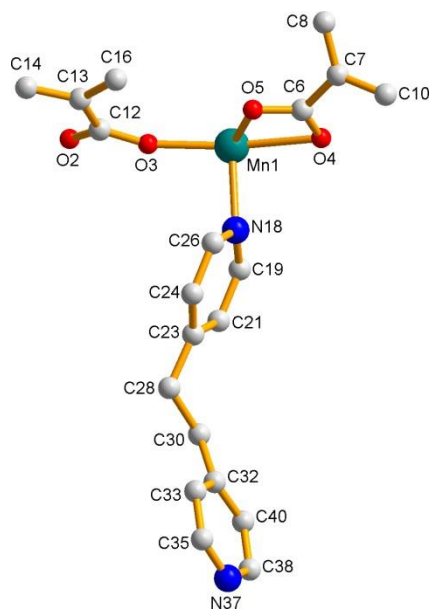
O4<sup>i</sup>—Mn1—N1 92.91(9) N1—Mn1—N2<sup>ii</sup> 176.78(9) N2<sup>ii</sup>—Mn1—O2 84.18(10)

O3—Mn1—O1 148.62(8) O1—Mn1—N2<sup>ii</sup> 89.04(10)

O4<sup>i</sup>—Mn1—O1 90.33(9) O3—Mn1—O2 90.74(8)

(i) 2-x, -y, -z; (ii) 1+x, y, 1+z; (iii) -1+x, y, -1+z; (iv) 2-x, 1-y, 1-z; (v) 3-x, 1-y, -z; (vi) 1-x, -y, -1-z.





Asymmetric unit for **2**.

Structural parameters for  $[\text{Mn}_2(\text{bdc})_2(\text{tpcb})]$ , **2**

Bond distances (Å)

Mn1—O2 2.233(15) Mn1—O4 2.382(41)

Mn1—O3 2.120(43) Mn1—O5 2.162(33)

Mn1—N18 2.262(19) Mn1—N37 2.277(23)

Bond angles (degrees)

N37—Mn1—N18 163.8(9) N18—Mn1—O5 96(1)

N37—Mn1—O2 82.3(9) N18—Mn1—O4 86.3(9)

N37—Mn1—O3 96(1) O2—Mn1—N18 82.2(8)

N37—Mn1—O4 87(1) O3—Mn1—O4 164(1)

N37—Mn1—O5 93(1) O3—Mn1—N18 95(1)

Table S5: Rietveld refinement parameters for **2**

Formula unit		C <sub>20</sub> H <sub>14</sub> N <sub>2</sub> O <sub>4</sub> Mn	
<i>Z</i>		2	
Space group		<i>P</i> $\bar{1}$	
<i>a</i> (Å)	10.0354(7)	$\alpha$ (°)	92.238(7)
<i>b</i> (Å)	10.8657(8)	$\beta$ (°)	98.521(5)
<i>c</i> (Å)	10.8045(9)	$\gamma$ (°)	121.811(5)
<i>V</i> (Å <sup>3</sup> )	980(4)		
Number of parameters refined	67(structure) 19(profile)	Profile Function	Split-Pearson VII
<i>R</i> <sub>wp</sub> (%)	3.64	<i>R</i> <sub>p</sub> (%)	2.66
<i>R</i> <sub>f</sub> (%)	6.75	GoF	1.54

## References

- (S1) Myers, A. L.; Prausnitz, J. M. *AIChE J.* **1965**, *11*, 121.
- (S2) (a) Babarao, R.; Hu, Z.; Jiang, J.; Chempath, S.; Sandler, S. I. *Langmuir* **2007**, *23*, 659. (b) Bae, Y.-S.; Mulfort, K. L.; Frost, H.; Ryan, P.; Punnathanam, S.; Broadbelt, L. J.; Hupp, J. T.; Snurr, R. Q. *Langmuir* **2008**, *24*, 8592.
- (S3) Krishna, R. *Micro. Meso. Mater.* **2014**, *185*, 30.
- (S4) Sato, H.; Kosaka, W.; Matsuda, R.; Hori, A.; Hijikata, Y.; Belosludov, R. V.; Sakaki, S.; Takata, M.; Kitagawa, S. *Science* **2014**, *343*, 167.
- (S5) Matsuda, R.; Kitaura, R.; Kitagawa, S.; Kubota, Y.; Belosludov, R. V.; Kobayashi, T. C.; Sakamoto, H.; Chiba, T.; Takata, M.; Kawazoe, Y.; Mita, Y. *Nature* **2005**, *436*, 238.
- (S6) Zhang, J.-P.; Chen, X.-M. *J. Am. Chem. Soc.* **2009**, *131*, 5516.
- (S7) Fischer, M.; Hoffmann, F.; Fröba, M. *ChemPhysChem* **2010**, *11*, 2220.
- (S8) Kim, H.; Samsonenko, D. G.; Yoon, M.; Yoon, J. W.; Hwang, Y. K.; Chang, J.-S.; Kim, K. *Chem. Comm.* **2008**, 4697.
- (S9) Noro, S.-i.; Tanaka, D.; Sakamoto, H.; Shimomura, S.; Kitagawa, S.; Takeda, S.; Uemura, K.; Kita, H.; Akutagawa, T.; Nakamura, T. *Chem. Mater.* **2009**, *21*, 3346.
- (S10) Yang, W.; Davies, A. J.; Lin, X.; Suyetin, M.; Matsuda, R.; Blake, A. J.; Wilson, C.; Lewis, W.; Parker, J. E.; Tang, C. C.; George, M. W.; Hubberstey, P.; Kitagawa, S.; Sakamoto, H.; Bichoutskaia, E.; Champness, N. R.; Yang, S.; Schroder, M. *Chem. Sci.* **2012**, *3*, 2993.
- (S11) Yanai, N.; Kitayama, K.; Hijikata, Y.; Sato, H.; Matsuda, R.; Kubota, Y.; Takata, M.; Mizuno, M.; Uemura, T.; Kitagawa, S. *Nat. Mater.* **2011**, *10*, 787.
- (S12) Eguchi, R.; Uchida, S.; Mizuno, N. *Angew. Chem. Int. Ed.* **2012**, *51*, 1635.
- (S13) Duan, X.; Zhang, Q.; Cai, J.; Yang, Y.; Cui, Y.; He, Y.; Wu, C.; Krishna, R.; Chen, B.; Qian, G. *J. Mat. Chem. A* **2014**, *2*, 2628.